

# The $^{21}\text{Na}(p, \gamma)^{22}\text{Mg}$ reaction from $E_{\text{c.m.}}=200$ to 1103 keV in novae and x-ray bursts

J. M. D'Auria,<sup>1</sup> R. E. Azuma,<sup>2</sup> S. Bishop,<sup>1,\*</sup> L. Buchmann,<sup>3</sup> M. L. Chatterjee,<sup>4</sup> A. A. Chen,<sup>5</sup> S. Engel,<sup>6</sup> D. Gigliotti,<sup>7</sup> U. Greife,<sup>8</sup> D. Hunter,<sup>1,†</sup> A. Hussein,<sup>7</sup> D. Hutcheon,<sup>3</sup> C. C. Jewett,<sup>8</sup> J. José,<sup>9,10</sup> J. D. King,<sup>2</sup> A. M. Laird,<sup>3,‡</sup> M. Lamey,<sup>1</sup> R. Lewis,<sup>11</sup> W. Liu,<sup>1</sup> A. Olin,<sup>3</sup> D. Ottewell,<sup>3</sup> P. Parker,<sup>11</sup> J. Rogers,<sup>3</sup> C. Ruiz,<sup>1</sup> M. Trinczek,<sup>3</sup> and C. Wrede<sup>1,§</sup>

<sup>1</sup>Simon Fraser University, Burnaby, BC, Canada

<sup>2</sup>University of Toronto, Toronto, Ontario, Canada

<sup>3</sup>TRIUMF, Vancouver, BC, Canada

<sup>4</sup>Saha Institute of Nuclear Physics, Calcutta, India

<sup>5</sup>McMaster University, Hamilton, Ontario, Canada

<sup>6</sup>Ruhr-Universität, Bochum, Germany

<sup>7</sup>University of Northern British Columbia, Prince George, BC, Canada

<sup>8</sup>Colorado School of Mines, Golden, Colorado 80401, USA

<sup>9</sup>Institut d'Estudis Espacials de Catalunya, UPC, Barcelona, Spain

<sup>10</sup>Universitat Politècnica de Catalunya, Barcelona, Spain

<sup>11</sup>Yale University, New Haven, Connecticut 06510, USA

(Received 12 February 2004; published 24 June 2004)

The long-lived radioactive nuclide  $^{22}\text{Na}$  ( $t_{1/2}=2.6$  yr) is an astronomical observable for understanding the physical processes of oxygen-neon novae. Yields of  $^{22}\text{Na}$  in these events are sensitive to the unknown total rate of the  $^{21}\text{Na}(p, \gamma)^{22}\text{Mg}$  reaction. Using a high intensity  $^{21}\text{Na}$  beam at the TRIUMF-ISAC facility, the strengths of seven resonances in  $^{22}\text{Mg}$ , of potential astrophysical importance, have been directly measured at center of mass energies from  $E_{\text{c.m.}}=200$  to 1103 keV. We report the results obtained for these resonances and their respective contributions to the  $^{21}\text{Na}(p, \gamma)^{22}\text{Mg}$  rate in novae and x-ray bursts, and their impact on  $^{22}\text{Na}$  production in novae.

DOI: 10.1103/PhysRevC.69.065803

PACS number(s): 25.40.Lw, 26.30.+k, 21.10.-k, 27.30.+t

## I. INTRODUCTION

Explosive stellar events, such as classical novae and x-ray bursts (XRB), are astrophysical sites wherein the “burning” of heavy elements can proceed by way of successive proton capture on radioactive nuclei. The high temperatures and densities within the burning zones of these events are such that radiative proton capture rates can exceed the competing beta decay rates of the reactant radioactive nuclei. Novae are presently understood to be the result of a thermonuclear runaway (TNR) on the surface of a white dwarf star within a binary star system. The fuel that feeds this runaway is hydrogen-rich material transferred from the companion star into the gravitational well of the white dwarf, resulting in a dense, hot, partially degenerate accreted envelope on the surface of the white dwarf. The H-rich accreted envelope mixes with the outermost layers of the underlying white dwarf which provides a source of “seed” CNO (or ONe) nuclei that power the explosion through proton capture reactions, initiating a TNR. The mechanism for an x-ray burst event is considered to be essentially that of a nova event, with the important distinction that the underlying progenitor of the explosion is a neutron star.

Nova temperatures and densities are such that, given Coulomb barrier constraints, the proton capture reaction flow predominantly occurs along the periphery of the proton-rich side of the valley of stability. With a neutron star as the underlying progenitor for x-ray bursts, burning zone temperatures and densities can be at least an order of magnitude greater than in novae, resulting in a reaction flow that occurs further removed from the valley of stability, even merging with the proton drip-line beyond  $A=38$  [1–3].

Above the proton threshold in the  $A=21$  mass region, nuclear level densities are low and proton capture reactions, at nova ( $T_9 \leq 0.4$ ) and x-ray burst temperatures ( $T_9 \leq 2$ ), are generally dominated by capture into narrow, isolated resonances. Knowledge of the resonance energies of these states in the compound system is critical for direct measurements of resonant proton capture; the bombarding beam energy must be tuned to provide a center of mass energy equal to the resonance energy. In the  $^{21}\text{Na}+p$  compound system, three resonances at  $E_x=5.714$ , 5.837, and 5.962 MeV had been thought to contribute to the  $^{21}\text{Na}(p, \gamma)^{22}\text{Mg}$  reaction rate at oxygen-neon novae temperatures. Within these nova events, the production of the astronomical observable  $^{22}\text{Na}$  is sensitive to this rate, and thus, to the strengths of these three resonances. Higher energy states at  $E_x=6.046$ , 6.248, 6.323, 6.587, and 6.615 MeV, in addition to the state at 5.962 MeV, may contribute to the  $^{21}\text{Na}(p, \gamma)^{22}\text{Mg}$  rate for x-ray burst events.

This paper is an extension to a previous radioactive beam study [4] which reported the resonance strength of the  $^{21}\text{Na}(p, \gamma)^{22}\text{Mg}$  reaction populating the  $^{22}\text{Mg}$  state at  $E_x$

\*Present address: Heavy Ion Nuclear Physics Laboratory, RIKEN, Wako, Saitama, 351-0198, Japan.

†Present address: Langara College, Vancouver, British Columbia, Canada.

‡Present address: University of York, York, England.

§Present address: Yale University, New Haven, CT 06510, USA.

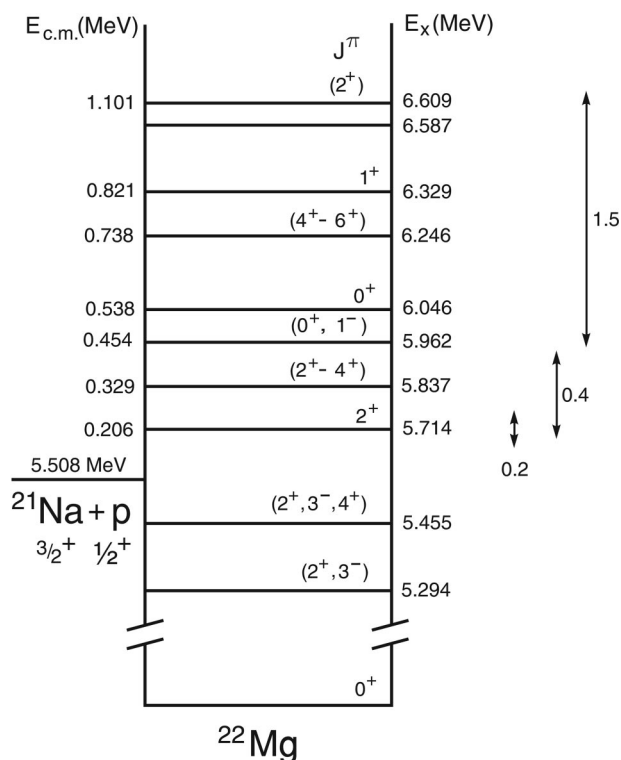


FIG. 1. Level scheme of the  $^{22}\text{Mg}$  nucleus showing the excitation energies (see text for discussion of the shown energies) and presumed spin assignments of the states of astrophysical interest. Gamow windows for  $^{21}\text{Na} + p$  burning are depicted on the right-hand side for some burning temperatures (in GK) typical of ONE novae or x-ray bursts. See text for discussion on the threshold energy shown.

$= 5.714$  MeV and its contribution to  $^{22}\text{Na}$  production in oxygen-neon novae. We report herein the experimental measurements of resonance strengths for the above mentioned resonances as determined from direct reaction yield studies using the DRAGON facility [5] at TRIUMF-ISAC [6]. From these experimental results we deduce the respective contributions of these states to the resonant  $^{21}\text{Na}(p, \gamma)^{22}\text{Mg}$  reaction rate, and their impact on  $^{22}\text{Na}$  production in ONE novae and XRB events.

## II. PREVIOUS $^{22}\text{Mg}$ STUDIES

Figure 1 shows our present understanding of the  $^{22}\text{Mg}$  level scheme with emphasis on states from the proton threshold to 6.6 MeV. Previous knowledge of the energy of the resonant states in  $^{22}\text{Mg}$ , near the proton threshold, was based on transfer reaction studies such as  $^{22}\text{Mg}(p, t)^{22}\text{Mg}$  [7,8],  $^{25}\text{Mg}(^3\text{He}, ^6\text{He})^{22}\text{Mg}$  [9], and  $^{12}\text{C}(^{16}\text{O}, ^6\text{He})^{22}\text{Mg}$  [10], along with several earlier studies summarized elsewhere [11]. Additionally, using the  $^{20}\text{Ne}(^3\text{He}, n\gamma)^{22}\text{Mg}$  reaction, an  $n$ - $\gamma$  coincidence study by Rolfs *et al.* [12] identified, with high precision, the first resonant state above the proton threshold in  $^{22}\text{Mg}$ , at  $E_x = 5713.9 \pm 1.2$  keV. Some of the above transfer reaction studies [7–10] had used this result as a calibration standard. Recently, elastic scattering studies with a radioac-

tive  $^{21}\text{Na}$  beam on hydrogen revealed further information on states above  $E_x = 6$  MeV [13,14]. The energies for the various states in Fig. 1 are taken from various sources including measurements from the present study. A more complete discussion can be found in Sec. VIII. The indicated threshold value is based upon a revised mass for  $^{22}\text{Mg}$ . The new threshold energy was obtained by taking the difference of the Rolfs *et al.* [12] direct excitation energy measurement of 5.714 MeV with the newly measured resonance energy in the recent study by Bishop *et al.* [4], as obtained by the low energy inflection point of a thick target yield curve. A revision of the  $^{22}\text{Mg}$  mass was recently corroborated [15].

Although much effort has been put into assigning the level spins of the  $^{22}\text{Mg}$  nucleus from triton angular distributions in  $(p, t)$  reactions [8], comparisons to states in the isospin analogue nucleus  $^{22}\text{Ne}$ , and transfer reactions exploiting natural [7,8,10] and unnatural [9] parity, little agreement has been thus far obtained for states above the proton threshold. Only the state at 5.714 MeV has been assigned a firm  $J^\pi = 2^+$  [11]. In a very recent review of this situation, Fortune *et al.* [16] attempted to clarify the situation but some questions still remain with respect to the spin assignments.

However, while knowledge on the spin-parity assignments of the astrophysically important resonant states in the  $^{22}\text{Mg}$  nucleus remains inconclusive, direct measurements of resonant proton capture into these states can determine their resonance strengths reliably, independent of their spin-parity assignments. We have done this for the states shown in Fig. 1 from  $E_x = 5.714$  MeV through to  $E_x = 6.609$  MeV.

## III. ASTROPHYSICAL IMPORTANCE OF $^{21}\text{Na}(p, \gamma)^{22}\text{Mg}$

### A. Classical nova outbursts

Classical novae are violent stellar events, whose energy release is only exceeded by gamma-ray bursts and supernova explosions. They are powered by thermonuclear runaways that take place on the white dwarf component of a close binary system (see Refs. [17–19], and references therein). Typically, they eject about  $10^{-4}$  to  $10^{-5} M_\odot$  per outburst, contributing to the enrichment of the interstellar medium in a handful of nuclear species, mainly  $^{13}\text{C}$ ,  $^{15}\text{N}$ , and  $^{17}\text{O}$ , plus traces of other isotopes such as  $^7\text{Li}$ ,  $^{20}\text{Ne}$ , or  $^{26}\text{Al}$ . Paramount interest has been focused on predictions of the potential gamma-ray line signatures associated with these explosions, a challenging feature that, due to the limited sensitivity achieved so far by gamma-ray detectors and the average distances of novae, has not yet been confirmed. One expected gamma-ray imprint of a classical nova outburst (see Refs. [20,21] and references therein) is the 1.275 MeV line associated with  $^{22}\text{Na}$  decay ( $t_{1/2} = 2.6$  yr). A few experimental searches for this  $\gamma$ -ray signal have been attempted in the last 25 years, including balloon-borne experiments [22], detectors on-board HEAO-3 [23] and SMM satellites [24], as well as both OSSE and COMPTEL experiments on-board CGRO [25,26]. Furthermore, ESA's recently launched INTEGRAL mission will also attempt to detect this unique gamma-ray feature both in the Core Programme as well as in the Guest Observer's Programme (see Hernanz *et al.* [21]). Up to now, only constraints on the overall amount of  $^{22}\text{Na}$  ejected into

the interstellar medium during nova outbursts have been derived from the former experiments. The most restrictive ones correspond to measurements performed with COMPTEL of five neon-type novae (Nova Her 1991, Nova Sgr 1991, Nova Sct 1991, Nova Pup 1991, and Nova Cyg 1992) [26] which led to an upper limit of  $3 \times 10^{-8} M_{\odot}$  of  $^{22}\text{Na}$  ejected by any nova in the Galactic disk.

The production of  $^{22}\text{Na}$  in novae has been extensively investigated in the last two decades (see Ref. [27], for a recent review), including parametric calculations [28–31], semianalytic [32,33] and hydrodynamic 1D models [18,19,34,35]. Its synthesis takes place by a combination of nuclear reactions in the NeNa cycle. Initially a thermonuclear runaway drives the outburst, proton-capture reactions occur on the “seed” nuclei  $^{20}\text{Ne}$  and these are responsible for significant amounts of the unstable nuclei  $^{21}\text{Na}$ . This is followed either by  $\beta^+$  decay of  $^{21}\text{Na}$  into  $^{21}\text{Ne}$  (“cold” NeNa cycle), which then leads to  $^{22}\text{Na}$  by means of  $^{21}\text{Ne}(p, \gamma)^{22}\text{Na}$ , or, for high enough temperatures, by proton captures on  $^{21}\text{Na}$  (“hot” NeNa cycle) leading to  $^{22}\text{Mg}$ . The  $^{22}\text{Mg}$  can then eventually decay into  $^{22}\text{Na}$ . Current theoretical models [36] for the nova explosion predict rather small amounts of  $^{22}\text{Na}$  in the ejected shells, below the upper limit derived by Iyudin *et al.* [26]. Nevertheless, such studies have also pointed out significant uncertainties of nuclear physics origin affecting critical rates involved in the synthesis (and destruction) of  $^{22}\text{Na}$ , among others,  $^{21}\text{Na}(p, \gamma)^{22}\text{Mg}$  and  $^{22}\text{Na}(p, \gamma)^{23}\text{Mg}$ . (See also Iliadis *et al.* [37], for an extensive study of nuclear uncertainties in nova nucleosynthesis.)

The uncertainty associated with  $^{21}\text{Na}(p, \gamma)^{22}\text{Mg}$  has been reduced recently as a result of our first experiment performed at the TRIUMF-ISAC facility [4]. This study was a direct measurement of the resonance strength of the  $E_x = 5.714$  MeV, the first level above proton threshold. The impact of this resonance on the rate of the  $^{21}\text{Na}(p, \gamma)^{22}\text{Mg}$  reaction rate and  $^{22}\text{Na}$  nucleosynthesis in nova outbursts was calculated and presented in Bishop *et al.* [4].

Recently, a different insight into the destruction rate of  $^{22}\text{Na}$  by the  $^{22}\text{Na}(p, \gamma)^{23}\text{Mg}$  reaction at ONE nova temperatures has been reported by Jenkins *et al.* [38] from  $\gamma$ -ray spectroscopy studies.

### B. Type I x-ray bursts

Type I x-ray bursts are cataclysmic events, characterized by a short burst duration ( $\sim 10$ – $100$  s), peak luminosities of about  $10^{38}$  erg  $\text{s}^{-1}$ , and recurrence times of a few hours (see Ref. [39], for a recent review). About 50 Galactic low-mass x-ray binaries that exhibit these bursting episodes have been found so far since the independent discovery by Grindlay *et al.* [40] and Belian *et al.* [41]. As pointed out by pioneering theoretical models [42,43], they are likely powered by thermonuclear runaways in the thin ( $d \sim 10$  m) H/He envelopes accreted on the neutron star component of a binary system. Due to the extremely high escape velocities from neutron stars, it is unlikely that any amount of envelope material might escape as a result of the explosion.

The most critical parameter in the specific characteristics of the burst is the mass accretion rate. In general, high mass

accretion rates ( $\dot{M} \sim 10^{-9} M_{\odot} \text{ yr}^{-1}$ ) involve combined hydrogen and helium burning whereas pure helium burning is expected at lower rates. In contrast, the type II subclass (up to now, consisting only of two objects, the so-called rapid burster MXB 1730-335, and the bursting pulsar GRO J1744-28) is not likely powered by thermonuclear runaways, and its origin is linked to accretion instabilities. Recently, a third class of erupting neutron stars, the so-called superbursts, has been discovered [44]: they exhibit strong bursts, about a thousand times longer and more energetic, and with much longer recurrent times ( $\sim$ years) than type I x-ray bursts. It has been suggested that superbursts are powered by unstable ignition in a pure C layer resulting from H/He burning [45].

Theoretical modeling of type I x-ray bursts has been extensively performed by different groups, usually in the framework of limited nuclear reaction networks due to computational limitations. Network endpoints include Ni [46,47], Se [48], Kr [49], or Y [47]. Moreover, calculations by Wallace and Woosley [47] reached  $^{96}\text{Cd}$ , but in the context of a reduced 16 nuclei network. On the other hand, Schatz *et al.* [3,50] have carried very detailed nucleosynthetic calculations, with a complete reaction network up to the SnSbTe mass region, but using a simple one-zone approach. An unprecedented attempt, coupling detailed hydrodynamic stellar models in one dimension (1D) with a complete nuclear reaction network (up to 1300 isotopes) has been recently performed [51].

The role of  $^{21}\text{Na}(p, \gamma)^{22}\text{Mg}$  in type I x-ray bursts is associated with one of the main nuclear paths followed during the course of the explosion, up to peak temperatures ( $T_9 \sim 1$ – $2$ ): at the typical densities attained at the base of the accreted envelope ( $\rho_b \sim 10^5$ – $10^6$  g  $\text{cm}^{-3}$ ), the nuclear activity is initiated by H burning (mainly CNO cycle), followed by He burning (initiated by the triple  $\alpha$  reaction). The rise in temperature is accompanied by a suite of CNO reactions involving radioactive reactants including possible breakout reactions,  $^{18}\text{Ne}(\alpha, p)^{21}\text{Na}$  or  $^{15}\text{O}(\alpha, \gamma)^{19}\text{Ne}$ , that extend the nuclear path through the NeNa region significantly through  $^{21}\text{Na}(p, \gamma)^{22}\text{Mg}$  and leading the way into the  $rp$  process, a combination of  $(p, \gamma)$ ,  $(\alpha, p)$ , and  $\beta^+$  decay reactions. Nuclear reactions leading to  $^{21}\text{Na}$  synthesis are  $^{20}\text{Ne}(p, \gamma)^{21}\text{Na}$  and  $^{21}\text{Mg}(\beta^+ \nu_e)^{21}\text{Na}$ . Further, there could be significant contribution from  $^{18}\text{Ne}(\alpha, p)^{21}\text{Na}$  and  $^{17}\text{F}(\alpha, \gamma)^{21}\text{Na}$ , that compete with destruction reactions such as  $^{21}\text{Na}(p, \gamma)^{22}\text{Mg}$  and  $^{21}\text{Na}(\beta^+ \nu_e)^{21}\text{Ne}$ . At the temperatures achieved during the course of the explosion for x-ray bursts ( $T_9 \sim 0.01$ – $2$ ) all levels from  $E_{\text{c.m.}}=200$  to 1103 keV contribute to the reaction rate, to some extent. It is worth noting that  $^{21}\text{Na}(p, \gamma)^{22}\text{Mg}$  is the main link from the CNO through the NeNa region and beyond, which stresses the relevant role played by this reaction in the evolution of the burst.

### IV. STELLAR REACTION RATE AND YIELD

In units of  $\text{cm}^3 \text{ s}^{-1} \text{ mol}^{-1}$ , the stellar reaction rate per particle pair for a narrow resonance,  $N_A \langle \sigma v \rangle$ , is given by [52],

$$N_A \langle \sigma v \rangle = 1.54 \times 10^{11} (\mu T_9)^{-3/2} \omega \gamma \exp\left(-11.605 \frac{E_R}{T_9}\right), \quad (1)$$

with  $N_A$  Avogadro's number;  $\mu$  the reduced mass, in  $u$ , of the compound system;  $T_9$  the temperature in units of GK;  $\langle \sigma v \rangle$  the thermally averaged nuclear cross section;  $E_R$  the resonance energy, and  $\omega \gamma$  the resonance strength, both in MeV. The resonance strength is defined by

$$\omega \gamma \equiv \frac{2J_R + 1}{(2J_p + 1)(2J_{21} + 1)} \frac{\Gamma_p \Gamma_\gamma}{\Gamma}, \quad (2)$$

with  $J_R$ ,  $J_p$ , and  $J_{21}$  the spins of the resonance, proton, and ground state of  $^{21}\text{Na}$ , respectively, and where  $\Gamma_p$  and  $\Gamma_\gamma$  are, respectively, the partial proton and partial gamma widths of the resonance. Last  $\Gamma = \Gamma_p + \Gamma_\gamma$ . Thus, it is seen from Eq. (1) that the resonant stellar reaction rate is directly proportional to the strength of the resonance through which radiative proton capture is occurring. Therefore, a measurement of  $\omega \gamma$  for a resonance in the compound system, of known energy, can play an important role in an understanding of a stellar reaction rate at a particular temperature.

The strengths of narrow isolated, resonances can be obtained from measurements of thick target yields. The resonant proton capture cross section,  $\sigma(E)$ , is given by the Breit-Wigner formula,

$$\sigma(E) = \frac{\lambda^2}{4\pi} \frac{2J_R + 1}{(2J_p + 1)(2J_{21} + 1)} \frac{\Gamma_p \Gamma_\gamma}{(E - E_R)^2 + (\Gamma/2)^2}, \quad (3)$$

with  $E$  the center of mass energy of the compound system,  $\lambda$  the de Broglie wavelength of the reduced mass of the compound system, and all other symbols as defined in Eqs. (1) and (2). Integration of Eq. (3) over a target thickness,  $\Delta E$ , gives the reaction yield per incident beam particle,  $Y$ . When  $\Gamma \ll E_R$ , a thick target yield curve is realized, given by [53], and

$$Y(E) = \frac{\lambda^2}{2\pi} \frac{m_{21} + m_p}{m_p} \left(\frac{1}{\rho} \frac{dE}{dx}\right)^{-1} \omega \gamma \left[ \arctan\left(\frac{E - E_R}{\Gamma/2}\right) - \arctan\left(\frac{E - E_R - \Delta E}{\Gamma/2}\right) \right], \quad (4)$$

where  $m_{21}$  and  $m_p$  are the  $^{21}\text{Na}$  and proton masses, respectively,  $dE/\rho dx$  is the laboratory-frame stopping cross section of  $^{21}\text{Na}$  through hydrogen, in units of energy loss per atom  $\text{cm}^{-2}$ , with  $\rho$  the hydrogen gas number density;  $E$  and  $\Delta E$  are the incident beam energy and total energy loss through the target in our system. The ratio of masses in Eq. (4) scales the stopping cross section into center of mass frame energy units. Equation (4) has a maximum when  $E = E_R + \Delta E/2$ , given by

$$Y_{\max} = \frac{\lambda^2}{\pi} \frac{m_{21} + m_p}{m_p} \left(\frac{1}{\rho} \frac{dE}{dx}\right)^{-1} \omega \gamma \arctan\left(\frac{\Delta E}{\Gamma}\right),$$

which, in the limit that  $\Gamma \ll \Delta E$ , becomes the thick target yield,

$$Y(\infty) = \frac{\lambda^2}{2} \frac{m_{21} + m_p}{m_p} \left(\frac{1}{\rho} \frac{dE}{dx}\right)^{-1} \omega \gamma, \quad (5)$$

with  $\lambda$  and  $dE/\rho dx$  to be evaluated at the resonance energy. A measurement, therefore, of thick target yield provides the resonance strength when the stopping cross section is known.

## V. EXPERIMENTAL FACILITIES

This reaction study was performed at the ISAC radioactive ion beam facility [6] at TRIUMF, located in Vancouver, Canada. A 500 MeV proton beam from the TRIUMF cyclotron, at  $\leq 30 \mu\text{A}$  intensity, bombarded a production target comprised of disks of specially prepared, powdered SiC. Spallation reactions on the silicon within the target material produced  $^{21}\text{Na}$  which diffused from the hot target and was ionized using heated surface ionization. Mass separation of the  $^{21}\text{Na}$  was performed using an initial low resolution pre-separator magnet followed downstream with a high-resolution dipole magnet. From here, the beam was directed into the ISAC room-temperature RFQ (radio frequency quadrupole) linear accelerator [6], exiting with an energy of 150 keV/nucleon. A thin carbon stripper was used to increase the charge state of the ion beam, which then entered the ISAC drift tube linac, with exit energies variable from 0.15 to 1.5 MeV/nucleon [6]. These accelerators produce a pulsed timing structure on the beam with a time spacing of 85 ns between particle bunches. The intensity of the  $^{21}\text{Na}$  beam delivered to DRAGON was  $\leq 10^9$   $^{21}\text{Na}$  per second.

The DRAGON (Detector of Recoils And Gammas Of Nuclear reactions) facility, situated in the ISAC experimental hall, consists of four main components: a differentially pumped, recirculating, windowless hydrogen gas target; a BGO  $\gamma$ -detector array; an electromagnetic mass separator (EMS); and a final focus heavy ion detector system. It has been designed to measure heavy ion radiative proton capture reactions at sub-Coulomb barrier energies in inverse kinematics. Figure 2 shows a schematic plan view of the DRAGON facility with major construction elements labeled. More complete description and details of the facility can be found in Ref. [5]; below is a summary of some of the main features.

The DRAGON gas target, elevation view shown in Fig. 3, consists of an aluminum target box in which is housed a windowless gas target cell (with an effective length of  $12.3 \pm 0.5$  cm). Recirculated hydrogen gas enters the target cell through an adjustable needle valve and exits by the upstream entrance and downstream exit apertures. The exiting  $\text{H}_2$  gas is pumped away with a system of Roots blowers, connected directly to the target box, and a battery of seven turbomolecular pumps (three upstream and four downstream of the target) to achieve high vacuum by differential pumping. The gas is compressed and sent to a liquid nitrogen cooled Zeolite trap for purification/cleaning before being returned to the gas cell. The gas charge contained within the Zeolite trap, in combination with the needle valve, were able to maintain target gas pressures stable to better than 1%. The target has been operated at pressures up to 10 Torr. The effective length of the target was determined in auxiliary mea-

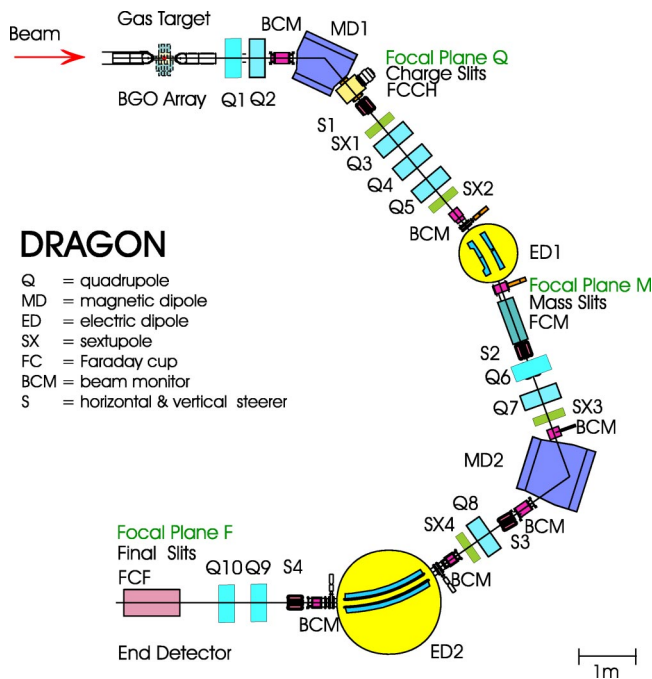


FIG. 2. (Color online) Schematic plan view of the DRAGON facility.

measurements with the regular entrance aperture (6 mm) and exit aperture (8 mm) replaced by apertures of 1.5 mm [54]. These measurements also validated a model based on empirical gas-flow equations, which estimated the pressure at the entrances to the pumping tubes to be approximately 1/15 of the pressure at the center of the cell.

Further details of the target can be found elsewhere [5]. Situated on the downstream side of the target cell, at  $30^\circ$  and

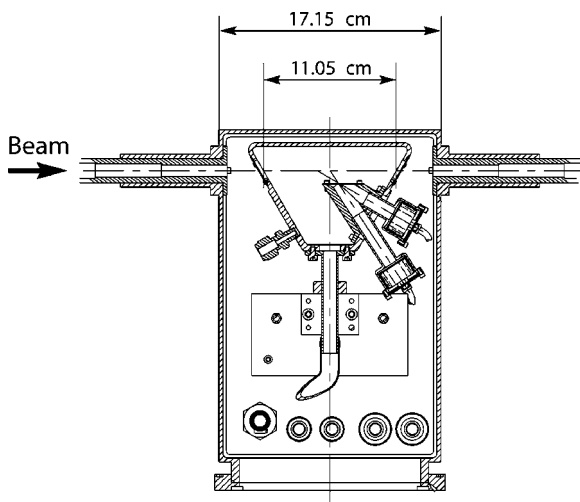


FIG. 3. Cut-away elevation view of the DRAGON target chamber containing the quadrangular inner gas cell. Situated on the left-hand wall of the cell is an opening to a capacitance manometer; on the right-hand wall are the two telescopes mounting the silicon detectors for monitoring elastically scattered protons. Pumping tubes are shown upstream and downstream of the target box. Hydrogen gas is admitted to the inner target cell through the tube attached to its bottom wall.

$57^\circ$  to the beam axis, are two collimated telescopes, to which are attached stations for mounting silicon detectors. Detectors mounted in these stations view a small length of gas located near the center of the gas cell and, therefore, detect elastically scattered protons caused by the passage of the  $^{21}\text{Na}$  through the  $\text{H}_2$  gas target. This provides one means by which Faraday cup readings taken upstream of the gas target are normalized to the total integrated beam on target. Only the detector at  $30^\circ$  was used for this experiment.

Surrounding the gas target box is a  $\gamma$ -detector array comprised of 30 BGO crystal detectors in a tightly packed geometry. The array covers approximately 90% of  $4\pi$  solid angle as viewed from the center of the gas cell, with about 50% efficiency for detection of the 5 MeV gamma ray using a 2 MeV threshold (see Sec. VII). The array readout is triggered by an energy deposition above a predetermined hardware threshold (usually 2 MeV, to suppress background from 511 keV annihilation photons) in one of the BGO detectors. The trigger gates ADC readout from all detectors having a deposited energy above the lower zero-suppression threshold. It also provides the start for a multihit TDC which receives stop signals from other BGO detectors (for gamma coincidences), the accelerator RF system, and the detector of heavy ion recoils (if any).

A separate data stream registered ADC and TDC information for the recoil ion detector, with a delayed version of the  $\gamma$  trigger supplied to one of the TDC channels. Data from this experiment therefore consisted either of coincidence events recognized by the presence of the  $\gamma$  (recoil) stop signal in the TDC, started by the recoil ( $\gamma$ ) trigger, or of singles events from only one of the triggers. Details of the array acquisition electronics and hardware can be found in Ref. [5], as can calibration and GEANT simulation results [55,56].

Following the gas target is a double-stage electromagnetic mass separator (EMS), 21 m in length from the center of the target cell to the location of the final focal plane detector. Each stage consists of a magnetic dipole and an electrostatic dipole bender, shown in Fig. 2. Fusion recoil and beam particles exit the gas target populating a distribution of charge states caused by electronic charge exchange collisions with the hydrogen molecules. In the first stage of the separator, a momentum dispersed focus after the first magnetic dipole (MD1) allowed passage of both beam and recoil ions of a *known* charge state through the remainder of the separator. The charge state chosen was the one for the fusion recoil,  $^{22}\text{Mg}$ , of highest probability at the particular energy of the reaction. Recoils and beam particles of charge states different from the selected charge state had their transmission blocked by slits, labeled as charge slits in Fig. 2. The charge state selection was based either on results from previous charge state studies [57,58], measured directly, or calculated (see below). The known charge state and momentum of the  $^{22}\text{Mg}$  recoils permits proper selection of magnetic and electric fields in the remainder of the EMS.

Following MD1, a quadrupole triplet in combination with the first electrostatic dipole bender, ED1, forms an achromatic focus at the location of the mass slits, as shown in Fig. 2. It is at this location where the first stage of mass separation takes place, as the electrostatic bender separates on the

basis of the kinetic energy difference between the fusion recoils and beam ions. This kinetic energy difference is determined by the ratio of the recoil and beam ion masses, and is  $\approx 5\%$  for  $^{21}\text{Na}$  and  $^{22}\text{Mg}$ . Adjustable slits were set to intercept the  $^{21}\text{Na}$  beam ions while allowing the  $^{22}\text{Mg}$  recoils to pass into the second stage of the EMS. A scintillator paddle, positioned upstream of these slits, monitored the  $\beta$ -decay of the intercepted beam and provided a second means by which to normalize the integrated beam on target.

After transport through the second stage of mass separation, using analogous principles to the first stage, fusion and beam ions were detected by a double-sided silicon strip detector (DSSSD), located at the final focal plane of the EMS. This detector measured the energy, and the horizontal and vertical position of ions impinging on it. Adjustable slits, forward of the DSSSD, in principle could be used for further beam background suppression, but were kept fully open for this study.

Faraday cups located just after the charge slits, mass slits, and final slits, along with beam centering monitors (BCM), provided the diagnostics necessary for optimally tuning the separator (with either a pilot stable beam of  $^{21}\text{Ne}$  or with the radioactive  $^{21}\text{Na}$  beam).

The beam energy was measured by adjusting magnetic dipole MD1 so as to center the transmitted beam on a 2 mm opening of the charge-selection slits at a focus downstream of MD1. Systematic studies with stable-beam capture reactions indicated that beam energies could be measured with a precision of 0.2% by this method. The method required careful positioning of beam on the ion-optical axis at the location of the gas cell. This was achieved in later stages of the experiment by means of a CCD camera which viewed the gas cell along the beam axis, imaging light produced by passage of beam through the gas cell. Good centering of the beam was important also for ensuring that the full cone of recoil particles would be transported through the downstream pumping tubes of the gas target. The trigger rate of the  $\gamma$ -detector array was very sensitive to beam spill at the target, providing a sensitive indication of beam motion during the course of a run.

## VI. EXPERIMENTAL METHOD

The ISAC beam direction and energy at the gas target were measured by a three step procedure: (1) the dipole, MD1, and quadrupoles, Q1 and Q2, were adjusted to focus the beam and center it through a 2 mm opening of the charge-state selection slits; (2) quadrupoles Q1 and Q2 were turned off and, if necessary, the beam direction from the ISAC accelerator was adjusted to recenter the beam at the slits at the same time requiring it to be on axis at the gas cell (as viewed by the CCD camera); and (3) a final determination of beam energy was made using the well-centered beam, by fine-tuning MD1 and converting its calibrated nuclear magnetic resonance (NMR) probe reading to beam energy [5,59]. This provided a precise measurement of the  $^{21}\text{Na}$  beam energy.

This procedure was performed either with gas removed from the target or, if the beam rigidity was greater than fa-

cility specifications, gas was introduced into the target chamber to generate higher charge states. Measurements at several reduced target pressures could be extrapolated to zero pressure to provide beam energy [59].

Next,  $\text{H}_2$  gas was admitted into the target, and the field of MD1 was scaled to accept the  $^{21}\text{Na}$  beam ions exiting the target with the recoil charge state of highest probability. The energy of the beam after passage through the gas target was determined as described above. This measurement was required for determining the  $^{21}\text{Na}$  stopping cross section, as required by Eq. (5), and for scaling the remaining EMS optics elements downstream of MD1 for this beam momentum and charge state. From this point, transport of the  $^{21}\text{Na}$  beam to the final focus typically involved using  $x$ - $y$  magnetic steerers and fine-tuning changes to the fields of ED1, ED2, and MD2. These small corrections were facilitated by diagnostic instruments that could be inserted into the path of the beam to determine its position relative to the beam axis, such as the mass slits downstream of ED1 and so-called beam centering monitors located immediately upstream of ED1, and immediately upstream and downstream of MD2 and ED2. Final focus slits, approximately 50 cm upstream of the DSSSD and  $x$ - $y$  steerers downstream of ED2, were employed for ensuring that the beam was on axis at the location of the DSSSD.

Upon completion of the  $^{21}\text{Na}$  beam transport to the final focal plane, scaling of the EMS optics tune for accepting  $^{22}\text{Mg}$  fusion recoils was a simple matter of scaling the electric potentials on ED1 and ED2 by  $m_{21}/m_{22}$ , the ratio of recoil ion mass to beam ion mass. Since these were the first ever measurements with DRAGON of unknown resonance strengths, a conservative approach was taken with regard to the mass and charge slit settings. The vertical and horizontal charge slits were set to 25 mm openings, as were the vertical mass slits; the horizontal mass slits were set to 15 mm and the final focus slits were always set fully open at 45 mm horizontally and vertically. These slit settings were selected based upon our optics calculations to ensure full recoil transmission through the separator and confirmed experimentally. In a separate study [59] using a stable beam, the strong  $^{21}\text{Ne}(p, \gamma)^{22}\text{Na}$  resonance at  $E_{c.m.} = 258.6$  keV was used to investigate possible loss of recoil ions at the horizontal mass slits, whose setting is crucial to reduction of beam background. This resonance has a recoil cone opening angle of 14.5 mrad, to be compared with 13.6 mrad or smaller for the resonances in  $^{21}\text{Na}(p, \gamma)^{22}\text{Mg}$ . Increasing the slit opening from 15 mm to 25 mm resulted in no increase in transmission of recoil ions, based on detection of about 500 coincidence events in each case. Separator transmission was investigated also in another study employing a magnetic steerer in place of the gas target to simulate recoil cone angle deflections. This work checked transmission through all parts of the system except the gas cell and the pumping tube closest to it, and found full transmission out to 17 mrad deflection of an incident beam.

As mentioned, the equilibrium charge state distributions of the recoiling  $^{22}\text{Mg}$  ions resulting from the gas in the target chamber was measured directly (if there was sufficient yield) or estimated from other measurements. Such measurements included equilibrium charge state distributions of the stable

beam,  $^{24}\text{Mg}$ , at beam energies of 200, 500, and 800 keV/nucleon for target pressures up to  $\approx 5$  Torr. The  $^{24}\text{Mg}$  beam was passed through the hydrogen gas target of sufficient thickness to ensure equilibrium [58], and a particular exiting beam charge state was selected by an appropriate field setting of MD1. Comparison of absolute beam current readings between a Faraday cup (FC) upstream of the target to that of a FC located just after the charge slits gave a measurement of that particular charge state fraction. This procedure was repeated for all other charge states by scanning through the appropriate fields in MD1 and comparing FC readings in the same manner. From this study it was found that the average equilibrium charge state,  $\bar{q}$ , could be estimated by an empirical relation of the form [57,58]

$$\bar{q} = Z_p \times \left[ 1 - \exp\left(-\frac{A}{Z_p^\gamma} \sqrt{\frac{v}{v'}} + B\right) \right], \quad (6)$$

where  $Z_p$  is the projectile atomic number,  $v$  the projectile velocity,  $v' = 3.6 \times 10^6$  m s $^{-1}$ , and  $A$ ,  $B$ , and  $\gamma$  are free parameters that were fitted to the charge state data, resulting in  $A=1.42$ ,  $B=0.45$ , and  $\gamma=0.445$  for  $\text{H}_2$  gas. This formula allows a calculated estimate of the charge state of highest probability for recoil ions with energies outside the energy range of previous charge state studies. Specifically, the equilibrium charge state distributions could be fitted well by a Gaussian profile parametrized by the mean charge state given by  $\bar{q}$  in Eq. (6) and an approximate width,  $d$ , characterized by  $d = d_1 Z_p^w$  with  $d_1=0.237$  and  $w=0.548$ . Using this calculated equilibrium charge state distribution, the equilibrium charge state fraction could be estimated. It should be noted that atomic shell effects are not taken into account. In practice, it was found that the distribution width is also determined by interpolation between previously determined experimental data values of width versus charge state for a given ion species [57,58].

## VII. DATA ANALYSIS AND RESULTS

A maximum likelihood analysis has shown that the experimental yield probability distribution function,  $P(r|Y)$ , is a Poisson distribution parametrically dependent on the various DRAGON facility efficiencies. It can be shown to be [60]

$$P(r|Y) = \frac{(\epsilon\eta\theta\delta f Y)^r}{r!} \exp(-\epsilon\eta\theta\delta f Y), \quad (7)$$

where  $r$  is the total number of  $^{22}\text{Mg}$  recoils detected,  $\epsilon$  is the  $\gamma$ -array efficiency,  $\eta$  is the selected  $^{22}\text{Mg}$  recoil charge state fraction for transmission through MD1,  $\theta$  is the EMS transmission efficiency, and  $\delta$  is the DSSSD efficiency. The factor  $f$  is the total number of incident  $^{21}\text{Na}$  ions as a fraction of  $10^{12}$ .

From Eq. (7), the maximum likelihood statistical estimator for the yield,  $Y_{\text{max}}$  is [60]

$$Y_{\text{max}} = \frac{r}{\epsilon\eta\theta\delta f}. \quad (8)$$

When  $r$  is large ( $r > 20$ ) the statistical error on the yield,  $\sigma_{Y_{\text{max}}}$ , is approximated by (Gaussian limit) [60],

$$\sigma_{Y_{\text{max}}} = \frac{Y_{\text{max}}}{\sqrt{r}}. \quad (9)$$

The  $1\sigma$  confidence interval,  $C_{1\sigma}$ , the probability that the true result lies between  $Y_{\text{max}} - \sigma_{Y_{\text{max}}}$  and  $Y_{\text{max}} + \sigma_{Y_{\text{max}}}$ , is 0.683.

For small  $r$ , however, the Poisson distribution of Eq. (7) is asymmetric about its maximum and, in general, must be numerically integrated in an interval about  $Y_{\text{max}}$  to determine the upper and lower limits of the  $1\sigma$  confidence interval on  $Y_{\text{max}}$  [60]. In this situation we require limits,  $a$  and  $b$ , satisfying the integral equation

$$C_{1\sigma} = \int_{Y_{\text{max}}-a}^{Y_{\text{max}}+b} P(r|Y) dY, \quad (10)$$

with  $a$  and  $b$  subject to the condition,

$$P(r|Y_{\text{max}}-a) = P(r|Y_{\text{max}}+b). \quad (11)$$

In the special case where no recoils are observed ( $r=0$ ), Eq. (7) reduces to an exponential and Eq. (10), with a lower limit of integration of zero, provides an analytical formula for the  $1\sigma$  upper limit on the yield,

$$Y \leq -\frac{1}{\epsilon\eta\theta\delta f} \ln(1 - C_{1\sigma}). \quad (12)$$

These equations form the basis for the narrow resonance, thick target yield results from 206 to 740 keV.

### A. Beam normalization

Determining the total integrated  $^{21}\text{Na}$  beam delivered onto the  $\text{H}_2$  gas target was done using the  $30^\circ$  elastic monitor detector in the gas target, or using the  $\beta$ -monitor scintillator paddle located at the mass slits just after ED1.

For the gas target elastic monitor, a correspondence between a beam current reading taken upstream of the gas target and the number of detected elastically scattered protons had to be determined. This was accomplished by measuring the total number of elastically scattered protons within a time window,  $\Delta t$ , in which the  $^{21}\text{Na}$  beam intensity was constant. An absolute normalization factor,  $R$ , between the beam current reading and the number of elastically scattered protons, is then given by

$$R = \frac{I/q}{e N_p E_{\text{beam}}^2 / P}, \quad (13)$$

where  $N_p$  is the number of elastically scattered protons within the  $\Delta t$  time window,  $I$  is the beam current as measured using a Faraday cup located  $\approx 2$  m upstream of the gas target,  $q$  is the charge state of the  $^{21}\text{Na}$  beam ions as delivered by the ISAC accelerators ( $5^+$ ),  $E_{\text{beam}}$  is the incident beam energy (keV/nucleon),  $P$  is the hydrogen gas pressure (Torr), and  $e = 1.602 \times 10^{-19}$  C.

The pressure and energy-squared factors enter this equation because elastic Rutherford scattering varies in direct proportion to pressure and inversely as the incident beam energy squared. This scaling makes the normalization factors invariant with respect to chosen target pressure and beam

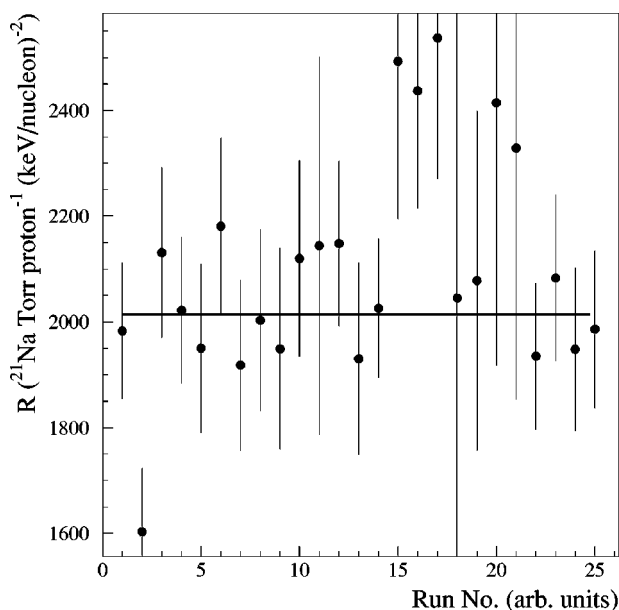


FIG. 4.  $^{21}\text{Na}$  beam normalization factors for various runs with a constant fitted to the data.

energy, provided the resonance is narrow in comparison to the beam energy spread. Figure 4 shows the set of normalization factors obtained for  $^{21}\text{Na}$  beam energies ranging from 210 keV/nucleon to 738 keV/nucleon and target pressures ranging from 4.5 to 8 Torr, along with a  $\chi^2$  fit of a constant  $R$  to the data. The dominant contribution to the error bars comes from the Faraday cup reading, which fluctuated at the level of  $\approx 7\%$  due to beam fluctuations and variations in visual cup readings (less important). The scaling factor obtained from the fit is

$$R = (2.014 \pm 0.035) \\ \times 10^3 \text{ }^{21}\text{Na} \cdot \text{Torr} / [\text{proton} \cdot (\text{keV/nucleon})^2].$$

The total integrated beam on target for a particular experimental run, at beam energy  $E_{\text{beam}}$  and target pressure  $P$ , is the above result multiplied by the total number of elastically scattered protons in the run after scaling them by  $E_{\text{beam}}^2/P$ .

In addition to the elastic monitor detector, a  $\beta$  scintillator monitor situated at the mass slits after ED1 can be used to measure the amount of  $\beta$  activity from the  $^{21}\text{Na}$  radioactive beam in the selected charge state. The position at which beam hits the mass slit is determined by the ratio of masses of beam and recoil ions, independent of the beam energy. For this experiment, the beam-recoil separation at the mass slit was about 2 cm. To calculate the amount of beam on target, the fraction of beam ions in the selected charge state must be known (see earlier discussion). Observed beam fluctuations between measurement of scattered beam into the elastic monitor detector and observed beta activity at the mass slits agreed very well.

### B. $\gamma$ -detector array efficiency

The efficiency response of the  $\gamma$ -detector array was modeled using the GEANT simulation software, and is the sub-

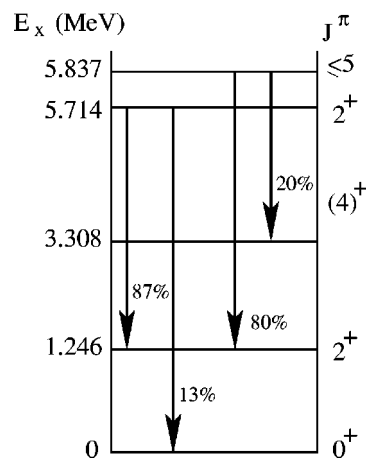


FIG. 5. Gamma cascade schemes (not drawn to scale) of the  $E_{\text{c.m.}}=206$  keV state ( $E_x=5.714$  MeV) and of the  $E_{\text{c.m.}}=329$  keV state ( $E_x=5.837$  MeV), with branching ratios and adopted spins shown.

ject of separate study [56]. The model incorporated the geometrical configuration of the array, gas target pumping box, gas target cell, and all materials comprising the target cell and pumping box, including the interactions of gamma rays with those materials. Within the simulation, an isotropic point source of  $\gamma$  rays was positioned along the beam axis, starting at  $z=-21.0$  cm (upstream of gas target center) and was stepped along the beam axis in increments of 2 cm. At each of these positions, the simulated source emitted  $\gamma$  rays with energies characteristic of the  $\gamma$ -decay schemes [12] of the 206 and 329 keV states. A diagram showing decay schemes of these two states is shown in Fig. 5.

In this way, the efficiency response of the  $\gamma$ -detector array was constructed for each branch of the two cascades of the 206 and 329 keV states [12]. The total efficiency of the array, for each state's cascade, was determined by taking the branching ratio weighted average of the individual branch response curves, and applying a simultaneous cut on the detected energy of  $E_\gamma \geq 3$  MeV. The total efficiency curves thus constructed are shown in Fig. 6. These simulation results have been validated with measurements using calibrated radioactive sources [56] and based upon these, a systematic uncertainty of 12% is universally adopted for all  $\gamma$ -efficiency values used in the present analysis. Because the resonances at 206 and 454 keV are narrow, the capture reactions took place in a length of target which depended mainly on the energy spread of the incident beam, corresponding to about 1 cm at the typical central pressures in the gas cell. From the pattern of hits in the elements of the array, it was possible to verify when the beam energy was such as to produce a resonance at or near the center of the cell. In order to calculate  $\omega\gamma$  it was necessary that the resonance be contained in the central region of the target, but detailed knowledge of the pressure profile was not necessary. The strengths reported for resonances at 539 keV and higher do not depend upon gamma-ray detection. The case of a resonance at 329 keV is discussed in a later section.

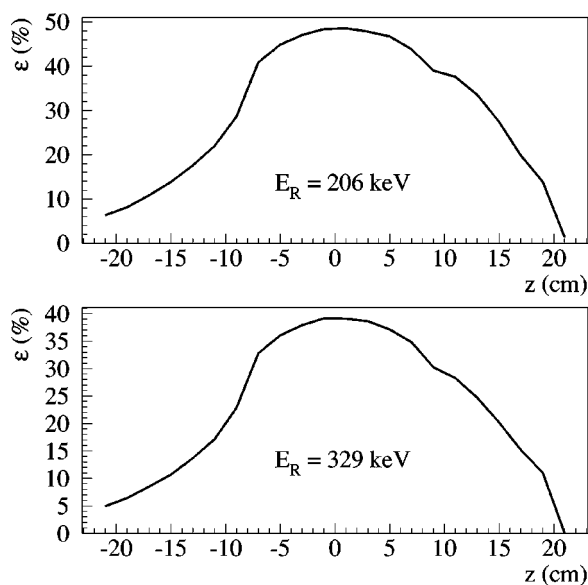


FIG. 6. The simulated  $\gamma$ -detector array total efficiency response,  $\epsilon$ , at 3 MeV threshold, for an isotropic point source as a function of position along the beam axis as determined by GEANT. Top panel, the response for  $\gamma$ -rays from the cascade of the state at 206 keV. Bottom panel, the response for  $\gamma$  rays from the cascade of the state at 329 keV. The asymmetry in both is caused by the presence of lead shielding upstream to minimize background from any beam hitting the upstream entrance pumping tubes and collimator.

### C. 206 keV resonance

The strength and yield of this resonance have been previously reported [4]. A summary of that analysis is provided here.

Using  $^{21}\text{Na}$  beam energies ranging from 210.8 to 230.8 keV/nucleon, a thick target yield curve for  $^{21}\text{Na}(p, \gamma)^{22}\text{Mg}$  was obtained. The gas target pressure used was typically 4.6 Torr, with the exception of one yield point, at  $E_{\text{beam}}=214.3$  keV/nucleon, where the target pressure was 2.5 Torr. For all data points,  $^{22}\text{Mg}$  recoil charge state equilibrium was assured as the critical target thickness to obtain  $^{22}\text{Mg}$  charge state equilibrium is calculated to be 4.4 mm (effective target length is 12.3 cm) at a target pressure of 4.6 Torr and 8.1 mm at 2.5 Torr, at these energies. This ensures that the recoil charge state fraction correction factor,  $\eta$ , in Eq. (8) is identical for all yield measurements of this resonance. Equation (6) predicts that the  $^{22}\text{Mg}$  recoil charge state of highest probability is  $4^+$ , and this was the recoil charge state selected for this yield study. Experimentally, the equilibrium charge state fraction of  $4^+$   $^{22}\text{Mg}$  was determined during stable beam commissioning studies employing the  $^{24}\text{Mg}(p, \gamma)^{25}\text{Al}$  reaction at  $E_{\text{c.m.}}=214$  keV/nucleon [59]. It was measured to be  $\eta=0.44$ , with a systematic uncertainty of 3%. By comparison, the calculated  $4^+$  charge state fraction is found to be  $\eta=0.41$ —a relative difference of 8% with experiment—and suggestive of the systematic error to use for recoil charge state fractions, not measured directly, of other resonance studies.

It was necessary to analyze the yield data of this resonance using  $\gamma$ -recoil coincidences. Figure 7 shows a heavy

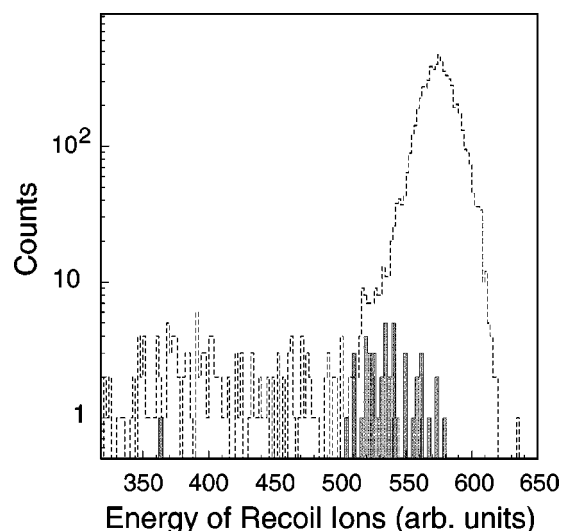


FIG. 7. DSSSD data from  $^{21}\text{Na}(p, \gamma)^{22}\text{Mg}$  at  $E_{\text{beam}}=220$  keV/nucleon. The dashed histogram shows the singles heavy ion energy spectrum from just one experimental run; it is dominated by  $^{21}\text{Na}$  unwanted beam ions passing through the separator. The filled histogram shows the corresponding total of all  $^{22}\text{Mg}$  recoil coincidence events from all runs at this beam energy. The low-lying  $^{22}\text{Mg}$  candidate at channel number  $\approx 362$  was rejected.

ion energy spectrum, in terms of channel number, obtained with the final focal plane DSSSD detector. The large dashed histogram is comprised of heavy ion singles data for a single run taken at a  $^{21}\text{Na}$  beam energy of 220 keV/nucleon. The bulk of the large peak and low energy tail consist of unseparated  $^{21}\text{Na}$  beam ions. Superimposed on the figure is the energy spectrum of all  $^{22}\text{Mg}$   $\gamma$ -recoil coincidence events from all runs at this beam energy. Beam ions would not be in coincidence with prompt reaction  $\gamma$  rays. The recoil events satisfy a nominal time of flight through the EMS of  $\approx 3.7 \mu\text{s}$  and a software cut on their corresponding  $\gamma$ -ray energy of  $E_{\gamma} \geq 3$  MeV. This software cut on the  $\gamma$ -ray energy was imposed to ensure that the  $\gamma$ -ray coincidence data used were unaffected by the pileup of 511 keV background from a very small amount of beam spill on the upstream target pumping tubes. A total of 45 recoil candidates occurs at this energy; however, the candidate event at channel number  $\approx 362$  was rejected on the basis of its anomalously low energy, leaving a total of 44  $^{22}\text{Mg}$   $\gamma$ -recoil coincidence events. These  $\gamma$ -recoil coincidence data correspond to the central thick target yield point in Fig. 4 of Bishop *et al.* [4];  $^{22}\text{Mg}$  recoil events for the remaining thick target yield points, of this figure, were obtained applying the same cut on detected  $\gamma$ -ray energies, but with corresponding shifts in cuts on the recoil time of flight arising from changes in the  $^{22}\text{Mg}$  recoil energy loss through the target, depending on the location of the reaction in the target.

These raw recoil coincidence events required efficiency correction factors to be applied to them [Eq. (8)]. Based on stable beam calibration reaction studies [59], a recoil EMS transmission efficiency of  $\theta=0.98 \pm 0.02$  is adopted for all yield data in this paper. In addition, an efficiency of  $\delta = 0.99 \pm 0.01$  for the final focal plane DSSSD detector was

measured [61,62] and has also been universally adopted in this paper. The  $\gamma$ -detector array efficiency response curve of Fig. 6 (top panel) provided the means by which to correct each yield point for the  $\gamma$ -detector array efficiency as a function of the reaction location within the gas target. For example, the data on the rising, low energy, flank of the yield curve must be resulting from a region near the entrance aperture of the gas target cell (at  $z=-5.5$  cm with respect to the center of the gas cell), suggesting an efficiency correction factor of 43%. The remaining yield data could then be individually corrected for the  $\gamma$ -detector array resonance position efficiency by applying a straightforward ratio relating the beam energy loss through the gas target and the known effective target length (12.3 cm) to the difference between the beam energy and resonance energy; i.e.,

$$z_{\text{res}} = \frac{12.3}{\Delta E_{\text{target}}} (E_{\text{beam}} - E_R^{\text{lab}}) \text{ cm}, \quad (14)$$

where  $\Delta E_{\text{target}} = 14.36 \pm 0.40$  keV/nucleon and  $E_R^{\text{lab}}$  is the resonance energy converted from the center-of-mass frame into the laboratory frame. Clearly, this relation only applies for narrow resonance reactions. The appropriate  $\gamma$ -efficiency factors were obtained from Fig. 6 using the computed values of  $z_{\text{res}}$ .

The yield curve in Fig. 4 of Bishop *et al.* [4] indicated a thick target yield of  $(5.76 \pm 0.88) \times 10^{-12}$  per incident  $^{21}\text{Na}$  ion. The  $^{21}\text{Na}$  energy loss through the gas target was measured to be  $(14.36 \pm 0.5)$  keV/nucleon corresponding to a stopping cross section of  $(8.18 \times \pm 0.41) \times 10^{-14}$  eV/(atom/cm<sup>2</sup>). A total integrated beam of  $(3.62 \pm 0.14) \times 10^{13}$  was delivered on target for this datum. These results, by Eq. (5), correspond to a resonance strength  $\omega\gamma = 1.03 \pm 0.16_{\text{stat}} \pm 0.14_{\text{sys}}$  meV. Last, the resonance energy, as indicated by the yield curve, was found to be at  $(205.7 \pm 0.5)$  keV, as discussed previously in Sec. II.

#### D. 329 keV resonance

The reaction study for this possible resonance, at  $E_x = 5.837$  MeV, employed a  $^{21}\text{Na}$  beam energy of 360 keV/nucleon and a nominal gas target pressure of 8 Torr. For these data, one run in the experiment was set to accept  $^{22}\text{Mg}$  recoils in a charge state of  $6^+$  while all other runs were set to accept  $5^+$  recoils. Charge state fractions of  $\eta_5 = 0.48 \pm 0.04$  and  $\eta_6 = 0.27 \pm 0.02$  are adopted for the  $^{22}\text{Mg}$  recoils of charge states  $5^+$  and  $6^+$ , respectively, on the basis of calculations from the model and data of Liu [57,58]. The assigned systematic error for each of these charge state fractions is taken as 8% as suggested in the preceding section.

Figure 8 shows the  $\gamma$ -recoil coincidence data for all runs. It can be seen that no  $\gamma$ -recoil coincidence events are observed for the expected  $^{22}\text{Mg}$  recoil time of flight. A resonance energy of 329 keV corresponds to a laboratory  $^{21}\text{Na}$  beam energy of 345 keV/nucleon, and the beam energy loss through the target was measured to be 28.2 keV/nucleon; over an effective target length of 12.3 cm due to the higher pressure. Thus, the position of a resonance reaction (at 329 keV) in the target would have been within approximately 1 cm of the center of the gas cell based upon data in

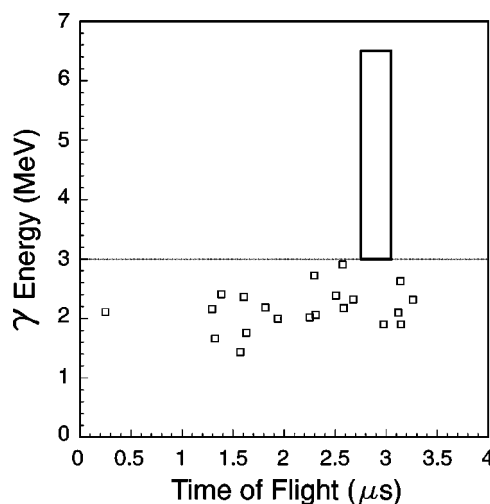


FIG. 8. Detected coincident  $\gamma$ -ray energy versus heavy ion time of flight of all data for the  $^{22}\text{Mg}$  resonance level at  $E_R = 329$  keV. The rectangular box indicates the location of the nominal time of flight of  $^{22}\text{Mg}$  recoils through the EMS. The horizontal dashed line denotes the  $E_\gamma = 3$  MeV energy cut. No valid recoil candidates are observed.

the literature [12]. The  $\gamma$ -detector array efficiency response curve, in the lower panel of Fig. 6, shows an efficiency of 0.38 within this range around the gas target center, assuming the decay scheme (Fig. 5) of Ref. [12]. The total integrated beam on target for the single run with the  $6^+$  recoil charge state selection was  $(4.50 \pm 0.14) \times 10^{11}$ ; for the  $5^+$  recoil charge state selection it was  $(8.65 \pm 0.87) \times 10^{12}$ . The stopping cross section of the beam was determined as  $(9.35 \pm 0.38) \times 10^{-14}$  eV/(atom/cm<sup>2</sup>).

These results, combined with the transmission and DSSSD efficiencies as discussed in the preceding section, result in a  $1\sigma$  upper limit on the yield of this resonance of  $7.36 \times 10^{-13}$ , where the inequality of Eq. (12) has been used. The combined systematic error that results from the uncertainties on all the efficiencies and beam measurements is  $1.19 \times 10^{-13}$ . A conservative upper limit on the yield of this resonance of  $8.55 \times 10^{-13}$  per incident  $^{21}\text{Na}$  ion is obtained by the linear sum of these two results. Consequently, an upper limit on the strength of this resonance of  $\omega\gamma < 0.29$  meV is obtained.

This state was originally identified on the basis of a  $\gamma$ -ray energy spectrum derived from a  $(^3\text{He}, n\gamma)$  transfer reaction measurement [12] but has not been confirmed in any other experiments, including an independent  $(^3\text{He}, n\gamma)$  measurement [63], four  $(p, t)$  transfer reaction studies [7,8,64,65], an  $(^{16}\text{O}, ^6\text{He})$  measurement [10], a  $(^3\text{He}, ^6\text{He})$  measurement [9], and a  $(^4\text{He}, ^6\text{He})$  measurement [66]; we have not observed it through this direct reaction study. The derived upper limit makes any such possible state irrelevant in the astrophysics context.

#### E. 454 keV resonance

This resonance was observed in a series of runs at beam energy  $490.0 \pm 0.9$  keV/nucleon with target gas pressure

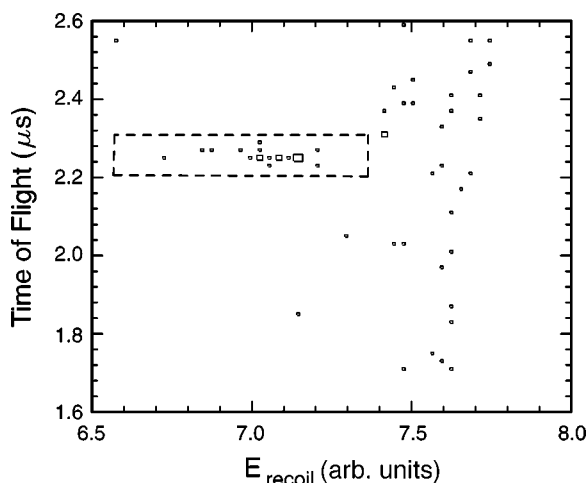


FIG. 9. Detected coincident heavy-ion energy versus time of flight of all runs for the  $^{22}\text{Mg}$  resonance level at  $E_R=454$  keV. The box indicates the region used to estimate yield of  $^{22}\text{Mg}$ .

8.0–8.2 Torr and the selected charge state  $6^+$ . The gamma-ray trigger threshold was set at 1.2 MeV. Based upon the position of the reaction in the extended target as observed from the gamma coincidences, the energy of the resonance was measured to be  $449 \pm 5$  keV.

A total of 20 events satisfied the combined cuts on recoil energy and time of flight (Fig. 9). A separate, wider time window in a region of accidental coincidences gave an estimate that  $0.4 \pm 0.2$  of the 20 events should be accidental. Plots of highest-energy gamma ray vs second-highest-energy gamma ray (if any) suggest the level has a major decay branch to the first excited state but, with a net yield of only 20 counts, significant branches to other levels cannot be ruled out. Because of the low gamma trigger threshold, it is extremely unlikely that a multistep cascade could “hide” 6 MeV of de-excitation energy from the gamma array. A  $\gamma$ -ray detection efficiency of 0.4 was assumed in the calculation of total yield.

Other factors entering the calculation of yield were fraction of beam in the selected charge state,  $0.38 \pm 0.04$ ; beam on target,  $4.9 \times 10^{13}$ ; stopping cross section,  $(1.02 \pm 0.05) \times 10^{-13}$  eV cm<sup>2</sup>/atom; recoil transmission/detection efficiency, 0.98. The result is a yield of  $1.7 \times 10^{-12}$  per incident  $^{21}\text{Na}$  ion and strength  $\omega\gamma=0.86 \pm 0.20(\text{stat})$  meV. The systematic error is estimated to be 25%, predominantly arising from gamma-ray detection efficiency due to lack of detailed knowledge of the branching ratios.

#### F. 538 and 738 keV resonances

For the reaction study of the  $^{22}\text{Mg}$  resonance at  $E_R=538$  keV, a beam energy of 570.2 keV/nucleon and gas target pressures of 4.8 and 7.6 Torr were employed. Additionally, data were also acquired using a beam energy of 582.7 keV/nucleon with a gas target pressure of 8.1 Torr. The selected  $^{22}\text{Mg}$  recoil charge state for the yield data acquired with the 4.8 Torr gas target pressure was  $6^+$ , whereas, for the data acquired at gas target pressures of 7.6 and 8.1 Torr, the selected  $^{22}\text{Mg}$  recoil charge state was  $7^+$ . The

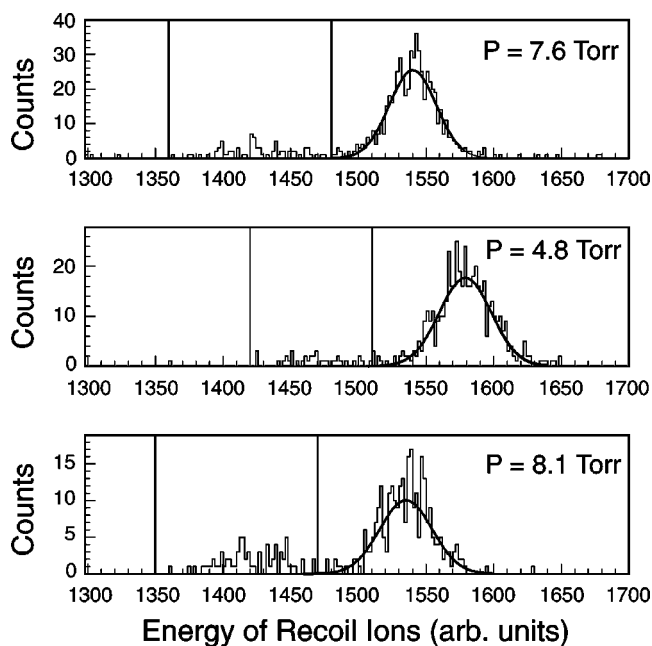


FIG. 10. DSSSD singles data for the  $^{22}\text{Mg}$  resonance level at  $E_R=538$  keV. The top panel shows the distribution of detected ion energies from runs taken at a target pressure of 7.6 Torr,  $E_{\text{beam}}=570$  keV/nucleon, and selected recoil charge state of  $7^+$ . The leaky beam peak, with Gaussian fit, is shown, along with the  $^{22}\text{Mg}$  fusion recoils, located between the two vertical lines. The central panel shows the same as the top panel, for all runs with a gas target pressure of 4.8 Torr, and selected recoil charge state of  $6^+$ . Finally, the bottom panel shows ion energies for a  $^{21}\text{Na}$  beam energy of 582.7 keV/nucleon, gas target pressure of 8.1 Torr, and a selected recoil charge state of  $7^+$ . Events within the region bounded by the vertical lines are taken as  $^{22}\text{Mg}$  recoils.

calculated equilibrium charge state fractions were determined as  $\eta_6=0.31 \pm 0.03$  and  $\eta_7=0.41 \pm 0.04$ .

Data analysis for these two resonances was done in singles mode, the  $^{21}\text{Na}$  beam suppression of the EMS, at these beam energies, having been sufficient to provide clear DSSSD  $^{22}\text{Mg}$  signals separable from the background leaky  $^{21}\text{Na}$  beam. As the  $\gamma$ -decay schemes for these two  $^{22}\text{Mg}$  states are unknown, this analysis approach obviated the use of the  $\gamma$ -detector array in the analysis along with its associated unknown efficiency response functions to the decays of these states.

Figure 10 shows the singles heavy ion energy spectrum, as measured by the DSSSD, for the yield study of the 538 keV resonance. The top panel of Fig. 10 shows all heavy ion singles data for runs taken with a nominal gas target pressure of 7.6 Torr and a selected recoil charge state of  $7^+$ ; the central panel shows all heavy ion singles for those data taken with a nominal gas target pressure of 4.8 Torr and a selected recoil charge state of  $6^+$ ; and the bottom panel shows all heavy ion singles for those data taken with a nominal gas target pressure of 8.1 Torr and selected recoil charge state of  $7^+$ . The prominent peaks within each panel, fitted with Gaussians, are the  $^{21}\text{Na}$  “leaky beam” (beam passing through the separator) energy distributions. The  $^{21}\text{Na}$  distribution for the data taken at a gas target pressure of 4.8 Torr

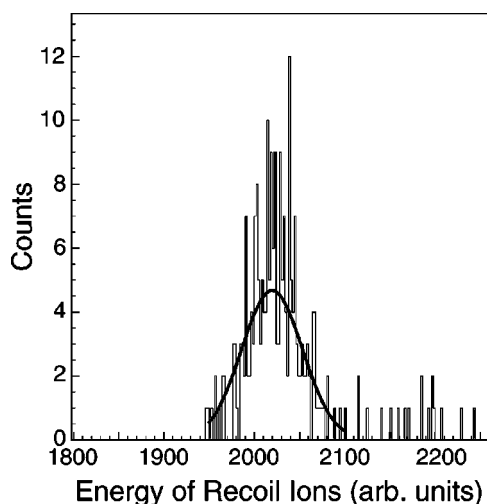


FIG. 11. DSSSD singles data for the  $^{22}\text{Mg}$  resonance level at  $E_R=738$  keV. The prominent peak is comprised of  $^{22}\text{Mg}$  recoil events. The few events above channel 2100 are  $^{21}\text{Na}$  “leaky beam” events.

is higher in energy due to the smaller beam energy loss in the gas target. The events located between the two vertical lines in each panel are taken as  $^{22}\text{Mg}$  recoil events. A total of 36  $^{22}\text{Mg}$  recoil events is observed in the data at 7.6 Torr gas target pressure; 75  $^{22}\text{Mg}$  recoil events are observed in the data at 4.8 Torr target pressure, and 72  $^{22}\text{Mg}$  recoil events are observed in the data at 8.1 Torr target pressure. The measured stopping cross section of  $^{21}\text{Na}$ , at these beam energies, was determined as  $(9.06 \pm 0.44) \times 10^{-14}$  eV/(atom/cm<sup>2</sup>).

With a total integrated beam on target of  $(1.50 \pm 0.10) \times 10^{13}$ , the thick target yield obtained from the  $6^+$   $^{22}\text{Mg}$  recoil data, after applying small dead-time corrections to the detected recoils, is determined to be,  $Y_{6^+} = (2.12 \pm 0.22_{\text{stat}} \pm 0.23_{\text{sys}}) \times 10^{-11}$  per incident  $^{21}\text{Na}$  ion. Consistent with this result, the dead-time corrected, thick target yield obtained from the  $7^+$   $^{22}\text{Mg}$  recoil data is determined as  $Y_{7^+} = (2.24 \pm 0.21_{\text{stat}} \pm 0.19_{\text{sys}}) \times 10^{-11}$  per incident  $^{21}\text{Na}$  ion, with a total integrated beam on target of  $(1.29 \pm 0.28) \times 10^{13}$ . Combining these results using the maximum likelihood result of Eq. (8) results in a derived thick target yield of  $Y = (2.19 \pm 0.15_{\text{stat}} \pm 0.20_{\text{sys}}) \times 10^{-11}$  per incident  $^{21}\text{Na}$  ion. The resulting resonance strength for the state in  $^{22}\text{Mg}$  at  $E_R = 538$  keV is  $\omega\gamma = 11.5 \pm 0.8_{\text{stat}} \pm 1.1_{\text{sys}}$  meV.

The study of the state previously observed at  $E_x = 6248.2$  keV [7] employed a fixed beam energy of 774.7 keV/nucleon and a nominal gas target pressure of 7.8 Torr. Based upon the position of the reaction in the extended target as observed from the gamma coincidences, the energy of the resonance was measured to be  $738.4 \pm 1.0$  keV. A single  $^{22}\text{Mg}$  recoil charge state of  $8^+$ , with a calculated charge state fraction  $0.43 \pm 0.04$ , was selected for this resonance study. Shown in Fig. 11 is the heavy ion energy spectrum, as detected by the DSSSD. The prominent peak in the spectrum contains  $^{22}\text{Mg}$  recoil events and the events above channel 2100 are  $^{21}\text{Na}$  “leaky beam” events. A total of 216  $^{22}\text{Mg}$  recoil events was observed for a total integrated beam on target of  $(1.67 \pm 0.07) \times 10^{12}$ . The resulting thick target

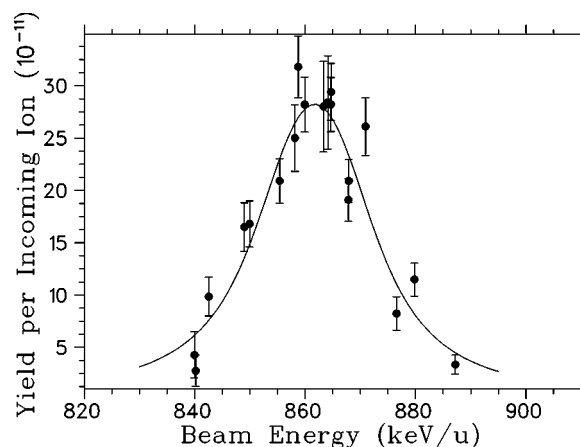


FIG. 12. The  $^{22}\text{Mg}$  experimental yield as a function of beam energy entering the gas target for the  $^{22}\text{Mg}$  resonance at  $E_R = 821$  keV. The displayed error bars are statistical and the curve is a least-squares fit of Eq. (4) to the data.

yield is  $(3.18 \pm 0.21_{\text{stat}} \pm 0.29_{\text{sys}}) \times 10^{-10}$  per incident  $^{21}\text{Na}$  ion, corresponding to a resonance strength,  $\omega\gamma$ , for the  $E_R=738$  keV state in  $^{22}\text{Mg}$  of  $(219 \pm 15_{\text{stat}} \pm 20_{\text{sys}})$  meV. The measured stopping cross section of  $^{21}\text{Na}$ , at these beam energies was determined as  $(8.74 \pm 0.39) \times 10^{-14}$  eV/(atom/cm<sup>2</sup>).

### G. 821 keV resonance

The resonance at  $E_R=821$  keV was studied over a range of 20 keV above and below the resonance energy. Data were analyzed in singles mode as the EMS provided suppression by a factor of  $\sim 10^{11}$  of the  $^{21}\text{Na}$  beam with respect to the recoiling reaction products. The number of observed recoil events depended on the probability of the charge state selected with the DRAGON recoil separator. This charge state probability was estimated by applying the empirical approach of Liu *et al.* [57,58]. While this approach agreed for tests done at beam energies of 230 keV/nucleon and 425 keV/nucleon, it did not for the resonance at 821 keV, where the charge state distribution was carefully measured for the recoils. A 20% discrepancy between the empirical approach and the measured value was observed. The measured recoil charge state fraction was used ( $7^+$ , 7.4%;  $8^+$ , 34.0%;  $9^+$ , 41.3%;  $10^+$ , 17.4%) and a systematic error of 10% was estimated.

The experimental yield curve obtained for this resonance is displayed in Fig. 12 along with a least-squares fit of the yield function of Eq. (4) to the data. While  $E_{\text{beam}}$ ,  $dE/\rho dx$ , and  $\Delta E$  were measured,  $E_R$ ,  $\Gamma$ , and  $\omega\gamma$  were set as free parameters in the fit. The error bars are statistical and were convoluted with an  $\approx 0.2\%$  error due to the uncertainty in the incoming beam energy.

To deduce the resonance widths from the fit parameter  $\Gamma$ , several contributions to the measured width had to be subtracted. According to previous work [59], these contributions are the (assumed) Gaussian energy spread of the beam, the broadening of the resonance due to energy straggling in the

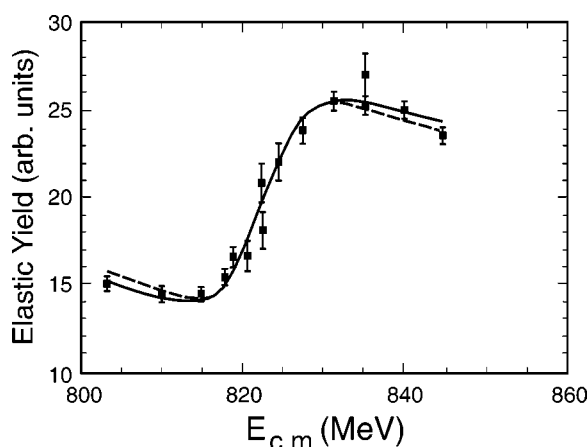


FIG. 13. Elastic monitor yields normalized to the beta monitor. The lines were obtained by folding an assumed Gaussian beam energy spread with the cross section for an isolated  $J=1$   $s$ -wave resonance at  $822.4 \pm 1.0$  keV. The solid line is for rms beam energy spread  $\sigma_E=1$  keV and  $\Gamma=18$  keV, the dashed line for  $\sigma_E=2$  keV and  $\Gamma=15$  keV.

target and the zero point motion of the  $\text{H}_2$  target molecules. The quadratic sum (3.0 keV/nucleon) of these functions was linearly subtracted from the fitting parameter to deduce the Lorentz-shaped natural width  $\Gamma$  [67]. This result was validated through simulation calculations which included beam energy uncertainty and straggling. From the resulting fit, the resonance strength was found to be  $\omega\gamma = 556 \pm 41_{\text{stat}} \pm 65_{\text{sys}}$  meV, the resonance energy  $E_R = 821.3 \pm 0.9$  keV, and the natural width  $\Gamma = 16.1 \pm 2.8$  keV, with a reduced chi-squared value of 2.3.

From the work of Ruiz *et al.* [68], where this resonance was first observed in  $^{21}\text{Na}+p$  elastic scattering, it was expected that the response of the elastic monitor counter would show substantial beam-energy-dependent deviations from that due to Rutherford scattering. For this reason, the beta monitor was used to determine the beam intensities for the calculation of radiative capture yields.

The ratio of counts in the  $30^\circ$  elastic scattering monitor to counts in the beta monitor gave a measure, to within an arbitrary constant, of the elastic scattering cross section at center-of-mass angle  $120^\circ$ . In contrast to the thick, solid  $(-\text{CH}_2)_n$  target of Ruiz *et al.* [68], the target viewed by our elastic monitor was pure  $\text{H}_2$  in which the beam lost only  $\approx 1$  keV/nucleon of energy. However, unlike the procedure in the thick-target analysis, each point in the present study required a new beam tune with an estimated uncertainty of 1–2 keV/nucleon in the measurement of each energy. Figure 13 shows the normalized yield from our elastic monitor as a function of beam energy.

The elastic monitor data are fitted with a total width  $\Gamma \approx 16$  keV, consistent with the value obtained from fitting the radiative capture yields where the target thickness was greater by an order of magnitude. This width is consistent also with the result obtained following detailed reanalysis of the thick-target data [13].

#### H. 1101 keV resonance

The data for the 1101 keV resonance in  $^{22}\text{Mg}$  were taken in the energy range of  $E_{\text{c.m.}} \approx 1090$  to 1135 keV and were

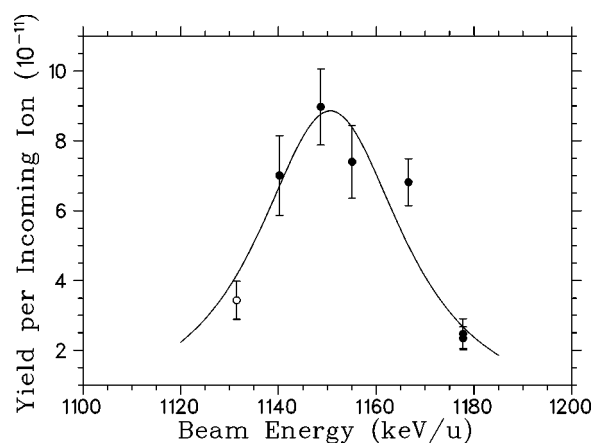


FIG. 14. The experimental yield curve of the 1101 keV resonance in  $^{22}\text{Mg}$  as a function of the beam energy entering the gas target. The solid curve is the resulting least-squares fit of the yield function of Eq. (4) to the data. The lowest energy point is believed to be influenced by a neighboring resonance and consequently was not included in the fit; see text for discussion.

analyzed in singles mode in a manner similar to that for the 821 keV resonance.

Figure 14 shows the experimental yield curve for the 1101 keV resonance in  $^{22}\text{Mg}$  plotted as a function of incoming beam energy. A least-squares fit of Eq. (4) to the yield function was performed, allowing the extraction of  $\omega\gamma$ ,  $E_R$ , and  $\Gamma$ . The displayed error bars are statistical and were used to weight the initial fit before the convolution with a 0.2% error due to the uncertainty in the measured beam energy.

There is another resonance nearby, about 20 keV lower in energy ( $E_R=1079 \pm 8$  keV and  $\Gamma=9 \pm 3$  keV [13]), that is believed to overlap with the low-energy tail of the 1101 keV resonance. Since the data in this energy region were incomplete, it was not possible to include the contribution from this neighboring resonance in the fit. Consequently, the lowest measured energy data point, while shown in Fig. 14, was not included in the fit of the 1101 keV resonance. The reduced chi-squared value for the final fit was 1.44 and the resonance strength was found to be  $\omega\gamma=368 \pm 47_{\text{stat}} \pm 41_{\text{sys}}$  meV at a resonance energy of  $E_R=1101.1 \pm 2.5$  keV. The natural width of  $\Gamma=30.1 \pm 6.5$  keV was determined by subtracting from the fitted width the contributions due to the energy spread of the beam, energy straggling and zero point motion, as elaborated above in the discussion of the 821 keV resonance. Further experimentation exploring gamma branching from these states will be employed to clarify this region.

#### I. Results

Table I summarizes the results of this analysis. Errors on  $\omega\gamma$  are the combined (in quadrature) statistical and systematic errors.

As indicated earlier, the energies of the states above threshold as displayed in Fig. 1 and presented in Table I requires some clarification. The state at  $E_x = 5713.9 \pm 1.2$  keV is given in Endt [11] as measured through direct gamma emission to the ground state by Rolfs *et al.*

TABLE I.  $^{21}\text{Na}(p, \gamma)^{22}\text{Mg}$  resonance strengths and energies.

$E_x$ (MeV)	$E_{c.m.}$ (keV)	$\Gamma$ (keV)	$\omega\gamma$ (meV)
5.714	$205.7 \pm 0.5$		$1.03 \pm 0.21$
5.837	329		$\leq 0.29$
5.962	$454 \pm 5$		$0.86 \pm 0.29$
6.046	$538 \pm 13$		$11.5 \pm 1.36$
6.246	$738.4 \pm 1.0$		$219 \pm 25$
6.329	$821.3 \pm 0.9$	$16.1 \pm 2.8$	$556 \pm 77$
6.609	$1101.1 \pm 2.5$	$30.1 \pm 6.5$	$368 \pm 62$

[12] while the corresponding  $E_R = 205.7 \pm 0.5$  keV was measured using DRAGON [4]. For  $E_R = 738.4 \pm 1.0, 821.3 \pm 0.9$ , and  $1101.1 \pm 2.5$  keV, these are the present measurements, leading to the proposed values of  $E_x = 6246, 6329$ , and  $6609$  keV, respectively, when combined with the new threshold value. The proposed energies are consistent with recent studies [9,10]. The values of  $E_x = 5961.9 \pm 2.5$  and  $6045.6 \pm 2.9$  keV are taken from the studies by Bateman *et al.* [4] due to their smaller errors as compared with this study.

## VIII. DISCUSSION AND CONCLUSION

### A. ONe novae

Figure 15 displays the respective resonant rates for each of the seven  $^{22}\text{Mg}$  states populated in the  $^{21}\text{Na}(p, \gamma)^{22}\text{Mg}$  reaction for temperatures consistent with ONe novae and x-ray bursts; an upper limit is shown for the possible resonance at 329 keV. Also included in the figure is the total  $^{21}\text{Na}(p, \gamma)^{22}\text{Mg}$  resonant reaction rate.

It is evident from the results of our resonance strength measurements that the  $^{22}\text{Mg}$  states at  $E_x = 5.837$  and

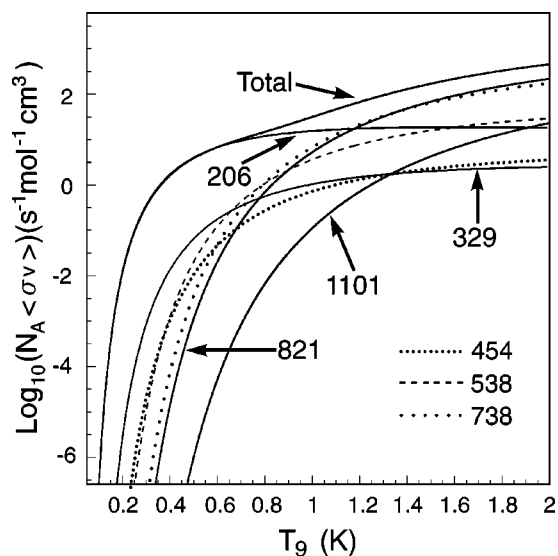


FIG. 15. Estimated reaction rate as a function of temperature based upon the resonances observed in this study; see text. The upper limit for the possible 329 keV resonance was plotted.

5.962 MeV are wholly insignificant for  $^{22}\text{Na}$  production in ONe novae and, indeed, will contribute negligibly to the  $^{21}\text{Na}(p, \gamma)^{22}\text{Mg}$  reaction path in x-ray burst events. The  $J^\pi = 2^+$   $^{22}\text{Mg}$  state at  $E_x = 5.714$  MeV ( $E_R = 205.7$  keV) is seen to be the dominant contributor to the  $^{21}\text{Na}(p, \gamma)^{22}\text{Mg}$  rate for the entire span of ONe temperatures, and is also seen to be the dominant contributor to the  $^{21}\text{Na}(p, \gamma)^{22}\text{Mg}$  rate up to temperatures of  $\approx 1.1$  GK. Only beyond 1.1 GK do the rate contributions from the resonances at  $E_R = 738$  keV and  $E_R = 821$  keV exceed that at  $E_R = 205.7$  keV. These conclusions are somewhat contradictory to the suggestion of Fortune *et al.* [16].

From a different perspective, the resonances at  $E_R = 821$  keV and  $1101$  keV could be considered too broad to use Eq. (4). According to the prescription of Ref. [69] these resonances would be considered narrow, having total widths less than 10% of their resonance energy. Nevertheless it was decided to use a broad resonance formalism in order to calculate the reaction rates, given that the total widths of these resonances probably far exceed that of the lower lying resonances. There is the possibility that the low-energy tail of one or both of these resonances could significantly contribute to the low temperature reaction rate. The total cross sections for these resonances was calculated according to the energy-dependent Breit-Wigner form of Ref. [69], and using a parametrization of the proton partial width in terms of the resonant proton width and the penetrability as

$$\Gamma_p(E) = \Gamma_p(E_R) \sqrt{\frac{E}{E_R}} \frac{P_\ell(E, r)}{P_\ell(E_R, r)}. \quad (15)$$

The proton width  $\Gamma_p(E_R)$  was set equal to the total width for each resonance. This would seem a reasonable assumption since the  $\gamma$ -ray widths for these states are likely to be very small. There was no inelastic strength observed in the 821 keV resonance in Ref. [13] further strengthening this assumption. The energy dependence of the  $\gamma$ -ray widths was treated in two different approaches, namely the first, assuming pure M1 transitions to the ground state for both resonances and setting the  $\gamma$  width on resonance to that of the  $1^+$  analogue state of the 821 keV resonance in  $^{22}\text{Ne}$  at 6854 keV; and the second, estimating a  $\Gamma_\gamma$  from the measured  $\omega\gamma$ . These are an approximation, and in order to calculate the reaction rate correctly at the very lowest temperatures, the  $(p, \gamma)$  cross section must take into consideration the energy dependence of the  $\gamma$  width at very low energies, where overlap integrals with the internal nuclear wave function begin to assume importance [70]. However, for our discussion of rates at nova temperatures and above, this approximation would seem to be valid. In other words, the resulting total reaction rate, calculated using a broad resonance formalism compared to the direct capture rate [7], and the rate calculated treating all resonances as narrow (the 821 and 1101 resonances were integrated using a Maxwell-Boltzmann approach) exhibit no significant difference over the temperature region associated with novae. In addition, although there is obvious deviation between these rates at temperatures below about 50 million degrees Kelvin, the direct capture rate dominates here. It is therefore concluded

that the treatment of the 821 keV and 1101 keV resonances as narrow Lorentzians is sufficient for calculation of the total reaction rate at nova temperatures.

The strength of the 205.7 keV resonance, as derived from this work, has been used as an input into the nuclear reaction network of an ONe nova model calculation [4]. The model employed was a spherically symmetric hydrodynamical one, incorporating an accreting  $1.25M_{\odot}$  ONe white dwarf, whose evolution is followed from the onset of accretion up to the explosion and ejection stages; it was the same model as one used previously [36]. The rates used for the total  $^{21}\text{Na}(p, \gamma)^{22}\text{Mg}$  reaction were identical to those used originally [36], the only difference being the use of our 205.7 keV resonance strength in place of the previous value. Abundance results of  $^{22}\text{Na}$  from the new calculation were compared to those of the original results of José *et al.* [36]. It was found that the  $^{22}\text{Na}$  mass fraction was reduced from  $3.5 \times 10^{-4}$  to  $2.8 \times 10^{-4}$ , using the  $\omega\gamma_{206}$  derived from this work [4]. Since the  $\omega\gamma_{206}$  of this work is higher than that used in the original model calculation [36], the  $^{21}\text{Na}(p, \gamma)^{22}\text{Mg}(\beta^+ \nu_e)^{22}\text{Na}$  synthesis path to  $^{22}\text{Na}$  is favored at earlier times in the outburst, reducing the role of the  $^{21}\text{Na}(\beta^+ \nu_e)^{21}\text{Ne}(p, \gamma)^{22}\text{Na}$  path. As a result,  $^{22}\text{Na}$  production occurs earlier in the outburst at a time when the expanding envelope is still sufficiently dense and hot to allow  $^{22}\text{Na}$  destruction from proton capture, reducing its final yield as compared with the previous calculation. While the previously adopted rates for the 329 and 454 keV resonances in the model of José *et al.* [36] are non-negligible compared to our newly derived results for these two resonance rates (Fig. 15), they are both completely dominated by our result for the rate of the  $E_{\text{c.m.}}=205.7$  keV rate, and, therefore, the overall reduction in the  $^{22}\text{Na}$  mass fraction will be insensitive to the addition from the rates used for the 329 and 454 keV resonances.

### B. x-ray bursts

We have analyzed the role played by  $^{21}\text{Na}(p, \gamma)^{22}\text{Mg}$  in explosions on neutron stars resembling type I x-ray bursts. For that purpose, we have computed two hydrodynamic sequences of models of  $1.4M_{\odot}$  neutron stars, accreting at a moderately high rate of  $1.75 \times 10^{-9} M_{\odot} \text{ yr}^{-1}$ . As shown recently [51] lower mass accretion rates ( $\sim 10^{-10} M_{\odot} \text{ yr}^{-1}$ ) lead to an early hydrogen depletion in the accreted envelope, before He ignition ensues ( $T \sim 0.2$  GK), and hence, limiting interest for the overall  $^{21}\text{Na}(p, \gamma)^{22}\text{Mg}$  rate to the levels above proton threshold. Therefore, in order to evaluate the effect of the high energy levels presented in this paper we have adopted a high value for the mass accretion rate, for which simultaneous H- and He-burning coexist during the course of the explosion towards peak temperature ( $\sim 1.2$  GK). Models have been computed by means of the spherically symmetric, hydrodynamic, implicit, Lagrangian

SHIVA code (see José and Hernanz [18], for details), adapted to neutron star conditions. The code incorporates an extended nuclear reaction network, consisting of 316 isotopes (ranging from  $^1\text{H}$  to  $^{60}\text{Ga}$ ) linked through a network of 2475 nuclear reactions (including proton, neutron, and alpha captures,  $\beta$  decays and the corresponding inverse reactions). Rates have been taken from the Brussels Netgen library [71].

Both hydrodynamic sequences are identical, the only difference being that whereas the full reaction network is included in the first model (hereafter, model A), the  $^{21}\text{Na}(p, \gamma)^{22}\text{Mg}$  rate is set to zero in the second one (model B), in an attempt to evaluate the specific role played by this reaction in the course of the explosion. The early evolution of the explosion is identical in both models, with a main nuclear activity focused in the CNO region. As soon as the temperature at the envelope's base reaches  $\sim 2.3 \times 10^8$  K, some leakage from the CNO region, by means of  $^{15}\text{O}(\alpha, \gamma)^{19}\text{Ne}(p, \gamma)^{20}\text{Na}$ , becomes progressively important, and paves the road towards the NeNa and MgAl regions, and beyond. When  $T$  exceeds  $3.5 \times 10^8$  K, the main nuclear path in model A passes right through  $^{21}\text{Na}(p, \gamma)^{22}\text{Mg}$ . On the contrary, evolution in model B proceeds through  $^{21}\text{Na}(\beta^+ \nu_e)^{21}\text{Ne}$ , because of the absence of the  $(p, \gamma)$  path. This fact induces some changes in the dominant path followed by both models up to  $^{24}\text{Al}$ , where the main path found in model A, initiated by  $^{21}\text{Na}(p, \gamma)^{22}\text{Mg}(p, \gamma)^{23}\text{Al}(p, \gamma)^{24}\text{Si}(\beta^+ \nu_e)^{24}\text{Al}$ , converges with that found for model B  $^{21}\text{Na}(\beta^+ \nu_e)^{21}\text{Ne}(p, \gamma)^{22}\text{Na}^{23}\text{Mg}(p, \gamma)^{24}\text{Al}$ . At this stage, it seems clear that the role of  $^{21}\text{Na}(p, \gamma)^{22}\text{Mg}$  is not critical, since the nuclear activity finds alternative paths on its way towards heavier species. However, we do find some differences in the overall evolution of the explosion. As a consequence of the two different paths (i.e., time scales, energy generation, etc.), the peak temperatures and luminosity achieved in the models are slightly different; whereas model A achieves a maximum temperature of  $1.20 \times 10^9$  K and  $L_{\text{peak}} = 1.14 \times 10^{38} \text{ erg s}^{-1}$ , model B achieves  $1.19 \times 10^9$  K and  $L_{\text{peak}} = 1.08 \times 10^{38} \text{ erg s}^{-1}$ .

### ACKNOWLEDGMENTS

The DRAGON group thanks the TRIUMF staff for their support. They are the hidden heroes that keep the facility going, particularly in the machine and electronics shops, computer support, beam lines, controls group, design office, cyclotron division, and the ISAC operations group. Special thanks go to the accelerator physicists, R. Laxdal, Z. Peng, and M. Pasini, for the tuning of the beam and M. Dombisky for the radioactive beam production. Financial support received from the Natural Sciences and Engineering Research Council of Canada, from the U.S. Department of Energy (DE-FG03-93ER40789 and DE-FG02-91ER40609), and from TRIUMF is gratefully acknowledged.

- [1] A. E. Champagne and M. Wiescher, *Annu. Rev. Nucl. Part. Sci.* **42**, 39 (1992).
- [2] F. Käppeler, F. K. Thielemann, and M. Wiescher, *Annu. Rev. Nucl. Part. Sci.* **48**, 175 (1998).
- [3] H. Schatz *et al.*, *Astrophys. J.* **524**, 1014 (1999).
- [4] S. Bishop *et al.*, *Phys. Rev. Lett.* **90**, 162501 (2003).
- [5] D. A. Hutcheon *et al.*, *Nucl. Instrum. Methods Phys. Res. A* **498**, 190 (2003).
- [6] R. E. Laxdal, International Workshop on the production of radioactive ion beams (PRORIB2001), Puri, India, 2001, URL: [http://www.triumf.ca/download/lax/prorib2000/prorib2001\\_paper%prorib2000\\_3.pdf](http://www.triumf.ca/download/lax/prorib2000/prorib2001_paper%prorib2000_3.pdf)
- [7] N. Bateman *et al.*, *Phys. Rev. C* **63**, 035803 (2001).
- [8] S. Michimasa *et al.*, *Eur. Phys. J. A* **14**, 275 (2002).
- [9] J. A. Caggiano *et al.*, *Phys. Rev. C* **66**, 15804 (2002).
- [10] A. A. Chen *et al.*, *Phys. Rev. C* **63**, 065807 (2001).
- [11] P. Endt, *Nucl. Phys.* **A521**, 1 (1990).
- [12] C. E. Rolfs *et al.*, *Nucl. Phys.* **A191**, 209 (1972).
- [13] C. Ruiz, Ph.D. thesis, University of Edinburgh, Edinburgh, Scotland, 2003, URL: [http://www.triumf.ca/dragon/docs/ruiz\\_phd.pdf](http://www.triumf.ca/dragon/docs/ruiz_phd.pdf)
- [14] C. Ruiz *et al.*, *Phys. Rev. C* **65**, 042801(R) (2002).
- [15] J. Hardy, *Phys. Rev. Lett.* **91**, 082501 (2003).
- [16] H. Fortune *et al.*, *Phys. Rev. C* **68**, 035802 (2003).
- [17] A. Kovetz and D. Prialnik, *Astrophys. J.* **477**, 356 (1998).
- [18] J. José and M. Hernanz, *Astrophys. J.* **494**, 680 (1998).
- [19] S. Starrfield *et al.*, *Mon. Not. R. Astron. Soc.* **523**, 178 (1999).
- [20] D. Clayton and F. Hoyle, *Astrophys. J.* **187**, L101 (1974).
- [21] M. Hernanz, *Classical Nova Explosions* (AIP, Melville, NY, 2002).
- [22] M. Leventhal *et al.*, *Astrophys. J.* **216**, 491 (1977).
- [23] W. Mahoney *et al.*, *Astrophys. J.* **262**, 742 (1982).
- [24] M. Leising *et al.*, *Astrophys. J.* **328**, 755 (1988).
- [25] M. Leising *et al.*, *Astron. Astrophys., Suppl. Ser.* **97**, 299 (1993).
- [26] A. F. Iyudin *et al.*, *Astron. Astrophys.* **300**, 422 (1995).
- [27] J. José, *Classical Nova Explosions* (AIP, Melville, NY, 2002).
- [28] W. Hillebrandt, *Astrophys. J.* **225**, 617 (1982).
- [29] M. Wiescher *et al.*, *Astron. Astrophys.* **160**, 56 (1986).
- [30] A. Weiss and J. W. Truran, *Astron. Astrophys.* **238**, 178 (1990).
- [31] A. Kudryashov *et al.*, *Astrophys. J.* **39**, 482 (1995).
- [32] N. A. Smirnova and A. Coc, *Phys. Rev. C* **62**, 045803 (2000).
- [33] S. Wanajo, M. Hashimoto, and K. Nomoto, *Astrophys. J.* **523**, 409 (1999).
- [34] M. Politano *et al.*, *Astrophys. J.* **448**, 807 (1995).
- [35] S. Starrfield *et al.*, *Astrophys. J., Suppl. Ser.* **523**, 178 (1999).
- [36] J. José, A. Coc, and M. Hernanz, *Astrophys. J.* **520**, 347 (1999).
- [37] C. Iliadis, A. Champagne, J. José, S. Starrfield, and P. Tupper, *Astrophys. J., Suppl. Ser.* **142**, 105 (2002).
- [38] D. Jenkins *et al.*, *Phys. Rev. Lett.* **92**, 031101 (2004).
- [39] T. Strohmayer and L. Bildsten, *Compact Stellar x-Ray Sources* (Cambridge University Press, Cambridge, in press).
- [40] J. Grindlay *et al.*, *Astrophys. J.* **205**, L127 (1976).
- [41] R. Belian *et al.*, *Astrophys. J.* **206**, L135 (1976).
- [42] S. Woosley and R. Wallace, *Nature* (London) **263**, 101 (1976).
- [43] L. Maraschi and A. Cavaliere, in *Highlights in Astronomy*, edited by E. Muller (Reidel, Dordrecht, 1977), Vol. 4, Part I, p. 127.
- [44] R. Cornelisse *et al.*, *Astron. Astrophys.* **357**, L21 (2000).
- [45] T. Strohmayer *et al.*, *Astrophys. J.* **566**, 1045 (2002).
- [46] R. E. Taam *et al.*, *Astrophys. J.* **413**, 324 (1993).
- [47] S. Woosley and R. Wallace, *High Energy Transients in Astrophysics* (AIP, New York, 1984).
- [48] T. Hanawa *et al.*, *Publ. Astron. Soc. Jpn.* **35**, 491 (1983).
- [49] O. Koike *et al.*, *Astron. Astrophys.* **342**, 464 (1999).
- [50] H. Schatz *et al.*, *Phys. Rev. Lett.* **86**, 3471 (2001).
- [51] S. Woosley *et al.*, *Astrophys. J.* (in press).
- [52] W. A. Fowler, G. R. Caughlan, and B. A. Zimmerman, *Annu. Rev. Astron. Astrophys.* **5**, 525 (1967).
- [53] W. A. Fowler, C. C. Lauritsen, and T. Lauritsen, *Rev. Mod. Phys.* **20**, 236 (1948).
- [54] U. Greife *et al.*, *Nucl. Instrum. Methods Phys. Res. B* **204**, 217 (2003).
- [55] D. G. Gigliotti, J. Rogers, and A. H. Hussein, *Nucl. Instrum. Methods Phys. Res. B* **204**, 671 (2003).
- [56] D. Gigliotti, Master's thesis, University of Northern British Columbia, Prince George, B.C., Canada, 2004.
- [57] W. Liu, Master's thesis, Simon Fraser University, Burnaby, B.C., Canada, 2001, URL: <http://www.triumf.ca/dragon/docs/wenjiethesis.pdf>
- [58] W. Liu *et al.*, *Nucl. Instrum. Methods Phys. Res. A* **496**, 198 (2003).
- [59] S. Engel, Ph.D. thesis Ruhr-Universität Bochum, Bochum, Germany, 2003, URL: [http://www.triumf.ca/dragon/docs/sabine\\_thesis.pdf](http://www.triumf.ca/dragon/docs/sabine_thesis.pdf)
- [60] S. Bishop, Ph.D. thesis, Simon Fraser University, Burnaby, British Columbia, 2003, URL: [http://www.triumf.ca/dragon/docs/bishop\\_phd.pdf](http://www.triumf.ca/dragon/docs/bishop_phd.pdf)
- [61] C. L. H. Wrede, Master's thesis, Simon Fraser University, Burnaby, B.C., Canada, 2003, URL <http://www.triumf.ca/dragon/docs/Wredethesis.pdf>
- [62] C. Wrede *et al.*, *Nucl. Instrum. Methods Phys. Res. B* **204**, 619 (2003).
- [63] H. Grawe *et al.*, *Nucl. Phys.* **A237**, 18 (1975).
- [64] R. A. Paddock, *Phys. Rev. C* **5**, 485 (1972).
- [65] B. Davids *et al.*, *Phys. Rev. C* **68**, 055805 (2003).
- [66] G. P. A. Berg *et al.*, *Nucl. Phys.* **A718**, 608c (2003).
- [67] G. Amsel and B. Maurel, *Nucl. Instrum. Methods Phys. Res.* **218**, 183 (1983).
- [68] C. Ruiz *et al.*, *Phys. Rev. C* **65**, 042801 (2002).
- [69] C. E. Rolfs and W. S. Rodney, *Cauldrons in the Cosmos* (University of Chicago Press, Chicago, 1988).
- [70] F. Barker and T. Kajino, *Aust. J. Phys.* **49**, 369 (1991).
- [71] A. Jorissen and S. Goriely, *Nucl. Phys.* **A688**, 508 (2001).